PCCP

PAPER

View Article Online
View Journal | View Issue

Open Access Article. Published on 07 November 2023. Downloaded on 3/15/2026 12:58:03 PM.
This article is licensed under a Creative Commons Attribution 3.0 Unported Licence.

Check for updates

Cite this: *Phys. Chem. Chem. Phys.*, 2023, **25**, 31848

Structural, electronic, optical, elastic, thermodynamic and thermal transport properties of $Cs_2AgInCl_6$ and $Cs_2AgSbCl_6$ double perovskite semiconductors using a first-principles study

Keqing Zhang,[a] Lijun Zhang,[a] S. K. S. Saravana Karthikeyan,[b] Chang Yi Kong,[bc] Fuchun Zhang,*[d] Xiang Guo,[e] Nam Nguyen Dang,[fg] Sankar Ganesh Ramaraj*[hi] and Xinghui Liu*[ej]

Received 9th August 2023,
Accepted 6th November 2023

DOI: 10.1039/d3cp03795a

rsc.li/pccp

In this study, we employ the framework of first-principles density functional theory (DFT) computations to investigate the physical, electrical, bandgap and thermal conductivity of $Cs_2AgInCl_6$-CAIC (type I) and $Cs_2AgSbCl_6$-CASC (type II) using the GGA-PBE method. CAIC possesses a direct band gap energy of 1.812 eV, while CASC demonstrates an indirect band gap energy of 0.926 eV. The CAIC and CASC exhibit intriguingly reduced thermal conductivity, which can be attributed to the notable reduction in their respective Debye temperatures, measuring 182 K and 135 K, respectively. The Raman active modes computed under ambient conditions have been compared with real-world data, showing excellent agreement. The thermal conductivity values of CAIC and CASC compounds exhibit quantum mechanical characteristics, with values of 0.075 and 0.25 W m^{-1} K^{-1}, respectively, at 300 K. It is foreseen that these outcomes will generate investigations concerning phosphors and diodes that rely on single emitters, with the aim of advancing lighting and display technologies in the forthcoming generations.

Introduction

Optoelectronics has recently seen a remarkable emergence of organic–inorganic hybrid halide perovskites ($APbX_3$), specifically $CH_3NH_3PbI_3$, due to their exceptional properties.[1–3] These properties include a favorable optical band gap, high photoluminescence quantum yield, elevated absorption coefficient, long carrier diffusion length, high carrier mobility, high tolerance to defects, and low manufacturing cost.[4–16] This rapid development and significant success have been unprecedented. Lead halide perovskite-based solar cells have shown a significant improvement in power conversion efficiency, ranging from 3.8% to an impressive 25.5%.[17–20] This significant advancement has attracted considerable attention within the scientific community, as these materials hold immense promise as potential replacements to conventional silicon-based solar cells. The remarkable photovoltaic properties of $CH_3NH_3PbI_3$ have been addressed through the convergence of experimental and theoretical investigations. These studies have demonstrated the crucial role that this compound's distinctive structural and electronic characteristics play.[21–26] Notably, the perovskite structure exhibits a remarkable degree of symmetry, which contributes significantly to its photovoltaic applications. Furthermore, the defect-tolerant nature of $CH_3NH_3PbI_3$ further enhances its photovoltaic performance. Additionally, the valence band edge is marked by strong coupling between the Pb-6s and I-5p orbitals, resulting in an antibonding interaction. Collectively, these features synergistically contribute to the exceptional photovoltaic properties observed in $CH_3NH_3PbI_3$. In the field of quantum physics, it is worth noting that the intrinsic thermodynamic instability of $CH_3NH_3PbI_3$ is probably grounded in the loosened chemical

[a] School of Chemical Engineering, Henan Technical Institute, Zhengzhou, Henan, 450042, P. R. China
[b] Department of Environment and Energy System, Graduate School of Science and Technology, Shizuoka University, 3-5-1 Johoku, Naka-ku, Hamamatsu 432-8561, Japan
[c] Department of Applied Chemistry and Biochemical Engineering, Faculty of Engineering, Shizuoka University, 3-5-1 Johoku, Naka-ku, Hamamatsu 432-8561, Japan
[d] School of Physics and Electronic Information, Yan'an University, Yan'an, 716000, China
[e] Science and Technology on Aerospace Chemical Power Laboratory, Hubei Institute of Aerospace Chemotechnology, Xiangyang 441003, Hubei, China. E-mail: guoxiang@casc42.cn, liuxinghui119@gmail.com
[f] Future Materials & Devices Lab., Institute of Fundamental and Applied Sciences, Duy Tan University, Ho Chi Minh City, Vietnam
[g] The Faculty of Environmental and Chemical Engineering, Duy Tan University, Danang, Vietnam
[h] Department of Bioengineering, The University of Tokyo, 7-3-1 Hongo, Bunkyo-Ku, Tokyo 113-8656, Japan. E-mail: ramaraj@g.ecc.u-tokyo.ac.jp, sankarg27@gmail.com
[i] Department of Materials Physics, Saveetha School of Engineering, Saveetha Institute of Medical and Technical Sciences (SIMTS), Thandalam, Chennai – 602105, Tamilnadu, India
[j] Division of Research and Development, Lovely Professional University, Phagwara, 144411, India

 This journal is © the Owner Societies 2023

Open Access Article. Published on 07 November 2023. Downloaded on 3/15/2026 12:58:03 PM.
This article is licensed under a Creative Commons Attribution 3.0 Unported Licence.

bonding of the organic cation CH_3NH^{3+} and its inherent instability.[27–34]

Organic components and the harmful nature of lead (Pb^{2+}), which are both essential parts of the widely used halide-based organic–inorganic hybrid perovskites, make them chemically unstable, which is the biggest problem. Despite the advantageous attributes of the $CH_3NH_3PbI_3$ perovskite, including its cost-effective solution treatment, remarkable defect tolerance, and ability to emit light across the visible spectrum with adjustable properties, lead halide perovskite encounters important challenges.[35–38] These challenges include prolonged exposure to light, sensitivity to humidity, instability at elevated temperatures due to environmental factors, and the inherent toxicity of Pb^{2+} ions, which can accumulate biologically within ecosystems. These concerns arise because of the restriction of hazardous substances (RoHS) directive. The inherent constraints have significantly limited their practical applications.[39–42] The interesting matters of stability have attracted greater attention and have been partially overcome through the substitution of the organic cation with inorganic cesium ions. This development has inspired the scientific community to begin a search for metal halide perovskite compounds that possess similar photoelectric characteristics while simultaneously exhibiting non-toxicity and steadfastness.

In recent investigations, a new group of lead-free halide double perovskites (HDPs) has attracted considerable attention. These studies have shown remarkable attributes, including excellent endurance to environmental factors, inherent thermodynamic stability, and a smaller effective mass of carriers. The nontoxic double perovskites under consideration exhibit promising potential as photovoltaic absorbers, with the aim of replacing $APbX_3$ in halide perovskite solar cells.[43–48] Furthermore, these materials are being proposed as potential alternatives for various optoelectronic applications, including X-ray detectors, thermal neutral scintillators employed in nuclear monitoring applications, white emitting phosphors, and ultraviolet detectors.[49–52] HDP compounds have been successfully synthesized and observed in the historical world since the beginning of the 1970s. However, it is worth noting that the methodologies employed in these endeavors were limited in their different perspectives. Specifically, the synthesis of Pb-free HDPs, which exhibit a chemical formula denoted as $A_2B'B''Cl_6$, wherein the presence of one B'^{1+} and one B''^{3+} species effectively replaces the two harmful Pb^{2+} ions, has been a subject of great interest. The goal of these investigations is to produce nontoxic perovskite structures, thus allowing the way for safer and more sustainable materials. The HDP effectively categorizes these entities into two distinct classifications, namely, type I and type II, predicated upon the presence or absence of lone-pair electrons within the B′ cations. HDPs of Type-I, which are dependent upon B′ cations, exhibit an absence of s states housing lone pairs (s0). The manifestation of Type-II HDP is dependent upon the presence of B′ cations, characterized by the possession of s electrons in a lone-pair configuration (s2). Furthermore, the utilization of lead-free HDP compounds exhibits an excellent tendency towards ecological sustainability. For a comprehensive understanding of the research history pertaining to CAIC and CASC, a recent summary has been published, providing detailed insights.[53–55] These materials exhibit promising optoelectronic properties similar to those observed in lead-based organic–inorganic hybrid perovskites, thus making them potentially useful for various applications.[56–61]

In this study, we employ the framework of first-principles density functional theory (DFT) computations to investigate the complex aspects that include the structural features, electronic conductivity, optical properties, elastic constants, and thermodynamic and thermal conductivity attributes of the DP candidate materials $Cs_2AgInCl_6$-CAIC (type I) and $Cs_2AgSbCl_6$-CASC (type II). This endeavor is dedicated to exploring the physical properties of the material and its potential as an approach to thermal conductivity. Our comprehensive theoretical investigation was conducted employing density functional theory (DFT) within the generalized gradient approximation (GGA-PBE) framework to elucidate the complex relationship between the electronic structure, optical characteristics, independent elastic moduli, Poisson's ratio, anisotropy, hardness, average sound velocity, Grüneisen parameter, Debye temperature, and the fundamental origins underlying the remarkably low thermal conductivity of CAIC and CASC compounds. Lattice dynamics calculations were additionally performed to characterize the thermodynamic stability, Raman, and infrared phonons, mainly focusing on calculation of the entropy, enthalpy, free energy, and specific heat capacity of the CAIC and CASC compounds. The theoretical calculations were subjected to investigation of the experimental vibrational spectroscopy data relating to Raman and infrared measurements, revealing excellent consistency. The high-throughput calculation of elastic constants was effectively visualized through the utilization of the online ELATE analysis platform. In our investigation, we have successfully determined the fundamental properties of each material, investigating the complex state of orbital hybridization and the consequential charge transfer phenomena that underlie the development of chemical bonding behavior within the CAIC and CASC compounds.

Computational studies

The DFT calculations were elegantly executed utilizing the PAW pseudopotential method,[62] which has been skillfully incorporated into the esteemed CASTEP code (CAmbridge Serial Total Energy Package).[63] The supercell dimensions of the CAIC and CASC model configurations have been systematically enhanced until the single defect state attains complete localization, showing as a $2 \times 2 \times 2$ lattice unit, including a total of 10 atoms under the influence of periodic boundary conditions. We have employed exchange and correlation (xc) functionals, specifically the generalized gradient approximation with perdew–burke–ernzerhof (GGA-PBE), in our computational calculations. The complex interaction between the fundamental constituents of ion cores and valence electrons is carefully explained with norm-conserved pseudopotentials.[64] The pseudopotentials employed in this study consider the valence states of Cs-$5s^25p^66s^1$, Ag-$4s^24p^64d^{10}5s^1$, In-$5s^25p^1$, Sb-$5s^25p^3$, and Cl-$3s^23p^5$ shells. The process of geometry

Open Access Article. Published on 07 November 2023. Downloaded on 3/15/2026 12:58:03 PM.
This article is licensed under a Creative Commons Attribution 3.0 Unported Licence.

optimization was executed by employing the Broyden–Fletcher–Goldfarb–Shanno minimization procedure.[65] The spatial coordinates of the atomic configurations are relaxed through the utilization of an ionic Hellmann–Feynman force convergence criterion of 0.01 eV Å^{-1}, employing a conjugate gradient minimization algorithm. The Brillouin zone was probed, employing the Monkhorst–Pack *k*-point[66] grid of 2 × 2 × 2 for the purpose of optimizing the structures. In the sector of energy calculations, the quantum mechanical aspects come into play, where the total energy tolerance, stress, and ionic displacement appear themselves as 5.0 × 10^{-6} eV per atom, 0.01 eV Å^{-1}, 0.02 GPa, and 5.0 × 10^{-4} Å, respectively. In our calculations, the energy cutoff for the plane wave is established at 850 eV.

Results and discussion

The crystal lattices of CAIC and CASC compounds were face-centered cubic, with a space group of $Fm\bar{3}m$ (SG: #220, O_h^5).[67] The lattice length (*a*) for the CAIC and CASC systems was found to be 7.4195 Å and 7.606 Å, respectively. From a structural perspective, it is possible to divide the CAIC and CASC compounds into two distinct entities, wherein Ag and B″ are distributed in a random manner within the same Wyckoff site (representing a disordered state) and are positioned at non-equivalent sites (representing an ordered state). The distinction between the two crystalline configurations arises due to the emergence of the superstructure denoted as $Fm\bar{3}m$, originating from the fundamental cubic $Pm\bar{3}$m unit cell. Fig. 1 exhibits the three-dimensional arrangement of CAIC and CASC compounds. These compounds exhibit a configuration wherein layers are constructed with alternating corner-shared octahedrons, specifically $[AgCl_6]^{5-}$ and $[B''Cl_6]^{3-}$. The extensive region that includes these octahedrons is filled by a three-dimensional network featuring Cs cations at the A-site, which are positioned at the center of the cuboctahedral space. This arrangement gives rise to a rock-salt ordering structure.[68–70] The observed characteristics of this compound exhibit enhanced stability under the influence of various external factors such as light, moisture, and ambient air within a functional environment.[71–73] The luminescent phenomenon observed in these compounds is deeply connected to the presence of self-trapped excitons (STEs), which emerge because of the determined Jahn–Teller distortion exhibited by the $[AgCl_6]^{5-}$ octahedron.[74] Still, making a 1 : 1 ordered perovskite system, which has a structure like elpasolite, is very hard because of the complicated relationship between thermodynamic constraints and the difficult synthesis conditions that are needed to make it work.[75,76]

The octahedral lattice structure defines the interstitial space where the Cs^+ ions are located. It is observed that octahedra possess perfect O_h symmetry. However, due to the distinct bond lengths between Ag–Cl and B″–Cl, the dimensions of their corresponding octahedra exhibit variation. In relation to CAIC, the interatomic bonding between the silver (Ag) and chlorine (Cl) atoms has been found to be 2.792 Å, while for the indium (In) and chlorine (Cl) atoms, it is determined to be 2.455 Å. Therefore, it can be concluded that the octahedral structure

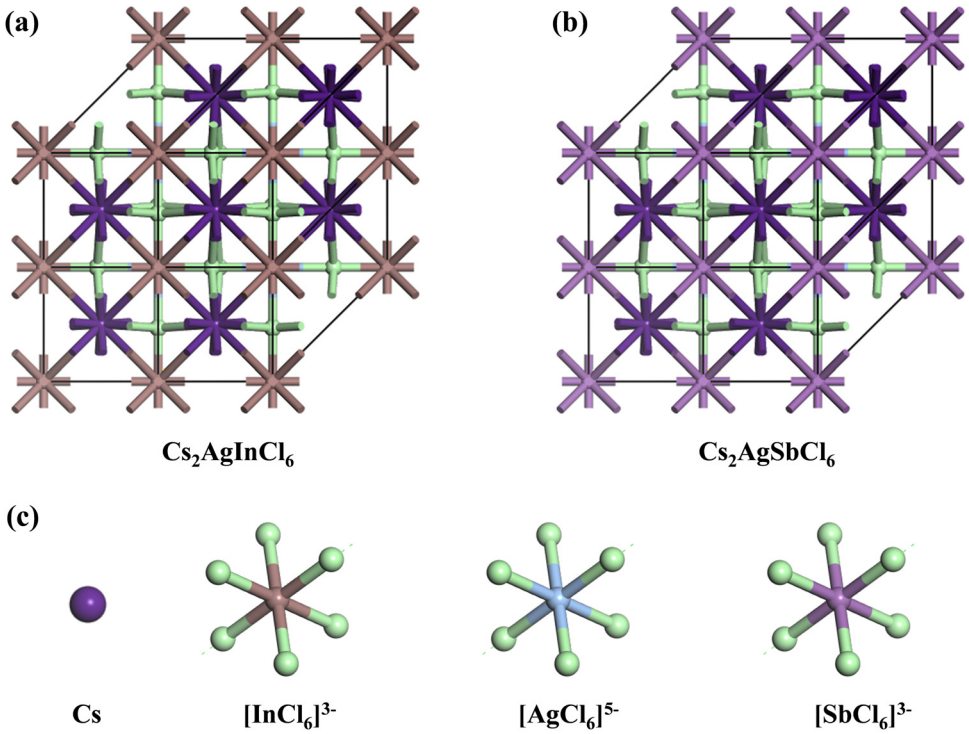

Fig. 1 (a) and (b) Double perovskite crystal structure of CAIC and CASC based DP, and (c) the crystal structure is composed of layers with alternating corner-shared $[AgCl_6]^{5-}$ and $[B''Cl_6]^{3-}$ octahedrons, and the large space located around the octahedrons is occupied by a 3D network with A-site Cs cations at the center of the cubeoctahedral space, which forms a rock-salt ordering structure.

Open Access Article. Published on 07 November 2023. Downloaded on 3/15/2026 12:58:03 PM.
This article is licensed under a Creative Commons Attribution 3.0 Unported Licence.

exhibited by the $[InCl_6]^{3-}$ species possesses a smaller size in comparison to the $[AgCl_6]^{5-}$ species. In connection with CASC, it is observed that the bond lengths between Ag and Cl atoms and Sb and Cl atoms were determined to be 2.755 Å and 2.624 Å, respectively. The lengths of the apical bonds (d_{abl}) and the equatorial bonds (d_{ebl}) are respectively given by[77]

$$d_{abl} = au\sqrt{2} \tag{1}$$

$$d_{ebl} = 0.5a\left[2(2u-1)^2+(c/a)^2\right]^{1/2} \tag{2}$$

where a and c are the lattice parameters and u are the positional parameters of the Cl atoms.

The chlorine position parameter (u), regarding bond lengths and tetragonality (c/a) can be expressed from eqn (1) and (2) and shortened to

$$u = 2d_{abl}{}^2 \pm d_{abl}\frac{\left[4d_{ebl}{}^2 + 2\left(d_{ebl}{}^2 - d_{abl}{}^2\right)(c/a)^2\right]^{1/2}}{4\left(d_{ebl}{}^2 - d_{abl}{}^2\right)} \tag{3}$$

Here, the estimations of d_{abl} and d_{ebl} are the same. The comparison between d_{abl} and d_{ebl} with average bond lengths ($0.5V^{1/3}$) is determined from the unit-cell volume V. The chlorine position parameter (u) for CAIC and CASC is 0.707 and 0.656 from eqn (3), respectively. Bond length, distances between octahedrons, volume, average bond lengths, and density are summarized in Table 1 for DP compounds. According to Shannon (SH) *et al.*[78] and Radaelli (Jahn–Teller, JT) *et al.*,[79] octahedral distortion (OD) is defined as

$$\Delta = \frac{1}{6}\sum\left(\frac{R_i - R_{av}}{R_{av}}\right)^2 \tag{4}$$

$$\sigma_{JT} = \sqrt{\frac{1}{3}}\sum\left[(MO)_i - (\langle MO\rangle)\right]^2 \tag{5}$$

where R_{av} and $\langle$M–O$\rangle$ are the average of six bond lengths in the octahedron and can be equal to $V^{1/3}$; R_i and $(M–O)_i$ are individual bond lengths in the MO_6 octahedron. SH and JT are calculated for CAIC and CASC and are 0.003×10^{-3} and 0.005×10^{-3}, as illustrated in Table 1. The OD presented by SH is more susceptible than that of JT, owing to changes in the bond length. So, the difference in the sizes of octahedra formed by $[AgCl_6]^{5-}$ and $[B''^{3+}Cl_6]^{3-}$, is higher in CAIC, followed by CASC.

Electronic structure

HDPs are mainly attributed to the inherent characteristics of the direct band gap, a phenomenon that has received growing interest after its insight by Yang *et al.*[80] and Volonakis *et al.*,[81] as well as the ground-breaking research conducted by Luo *et al.*[82] on their utilization as white light emitters. The successful experimental synthesis of HDP has yielded promising results in terms of its band gap properties. Specifically, the CAIC variant exhibits a direct band gap ranging from 3.3 to 3.5 eV, while the CASC variant possesses an indirect band gap within the range of 2.5 to 2.7 eV.[83–86] These band-gap characteristics make HDP suitable for utilization in photovoltaic applications. Additionally, it has been observed that HDP demonstrates a prolonged carrier lifetime and can be easily processed in solution form. However, it is important to note that HDP exhibits a low photoluminescence quantum yield (PLQY) of less than 0.1%, which can be attributed to the presence of parity-forbidden transitions.[87] The presented graphical representation in Fig. 2 exhibits the band structures of CAIC, CABC, and CASC, which have been resolved with respect to their orbital characteristics. These insightful findings have been derived from the authoritative ref. 87. GW-BSE calculations have also been used to determine that the exciton binding energy for CAIC is 0.25 eV, where G stands for the single-particle Green's function, W stands for the screened Coulomb interaction, and BSE stands for the Bethe–Salpeter equation.[88] The optical response in the visible region is not observed due to the wide band gap of HDP. So, the best way to reduce its band gap and widen its spectral response in the visible light domain may be to alloy it with the right parts. Interestingly, it has been previously documented that the process of alloying a metal cation, specifically lanthanide ions (Dy^{3+}, Sm^{3+}, Tb^{3+}), within these HDP materials contributes to the shifting of the energy difference between the valence and conduction bands and concurrently enhances the efficiency of photoluminescence.[89–93]

For CAIC and CASC, the band structure of the face-centered cubic phase was calculated along the lines connecting W, L, G, Z, W, and K. The band structure suggests that the valence band maximum (VBM) and the conduction band minimum (CBM) are located at W and K, the symmetry points, respectively. Fig. 3 shows the electronic band structure and density of states (DOS) of CAIC and CASC. The bandgap of CAIC and CASC is about 1.812 eV at the G-point (Fig. 3a) and 0.926 eV at the L-point (Fig. 3c). Therefore, CAIC acts as a direct and CASC acts as an indirect band gap semiconductor, and the use of the exchange correlation function provides a better result.[40] DOS provides information about the complex bonding of the materials and represents the electron–electron correlation effects in a unit cell. For CAIC, the VBM contributes mainly to the Ag-4d, Cs-5p, and Cl-3p orbitals, with a moderate contribution from the In-5s

Table 1 Calculated bond lengths (d), unit-cell volume (V), average bond length ($0.4958V^{1/3}$), and chlorine positional parameter (u) of DP compounds

	Bond length (Å)					Octahedral distortion (OD)	
HDP compound	Ag–Cl	B″–Cl	Volume (V) (Å)^3	$0.4958V^{1/3}$	u	Shannon[78] Δ ($\times 10^{-3}$)	JT[79]
$Cs_2AgB''Cl_6$ B″ = In	2.792	2.455	288.812	3.2773	0.2661	0.003	0.136
$Cs_2AgB''Cl_6$ B″ = Sb	2.755	2.624	311.140	3.3596	0.2561	0.005	0.211

Open Access Article. Published on 07 November 2023. Downloaded on 3/15/2026 12:58:03 PM.
This article is licensed under a Creative Commons Attribution 3.0 Unported Licence.

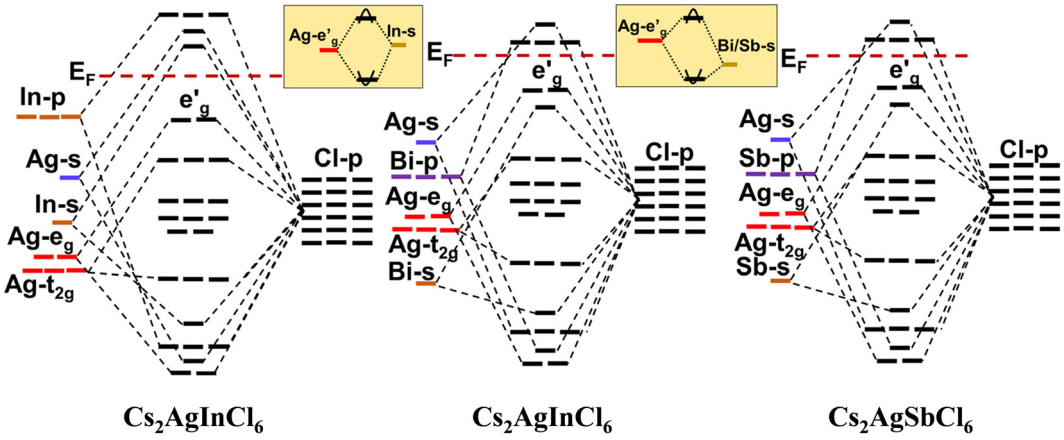

Fig. 2 The molecular orbital images were acquired through a review of the band structure of $Cs_2AgInCl_6$ (CAIC), $Cs_2AgBiCl_6$ (CABC), and $Cs_2AgSbCl_6$ (CASC) with an overview showing the predominant orbital attributes. The appearance of parity in the energy levels of the valence and conduction bands is effectively depicted through the utilization of Koster notation. In the inset, we observe a depiction of the hybridization process involving the hybridized Ag-eg orbitals and the In/Bi/Sb-s orbitals. This representation serves the purpose of identifying the configuration of the valence and conduction band edges' dispersion within these compounds. The intellectual property rights pertaining to the content mentioned in ref. 87 are hereby acknowledged.

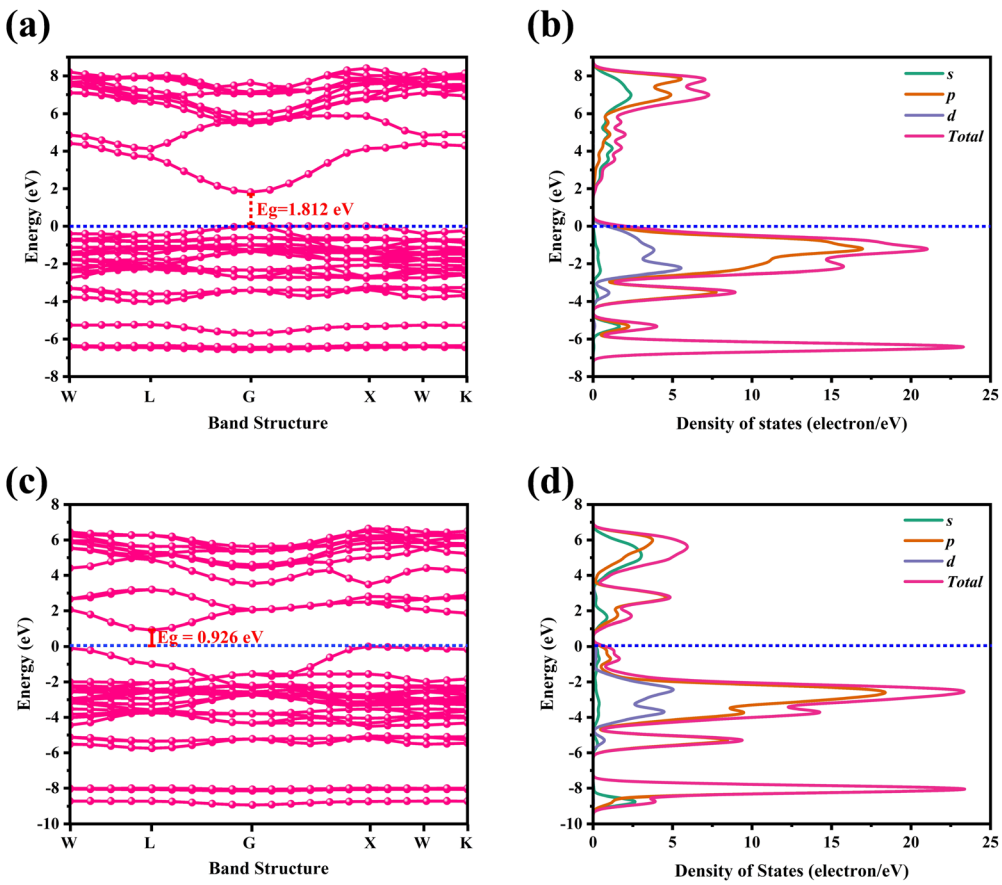

Fig. 3 Electronic band structure for CAIC and CASC compounds are calculated using the GGA-PPE method (a)–(c). In the DOS, CAIC exhibit direct band gap semiconductors, and CASC exhibit indirect band gap semiconductors (b)–(d).

and -5p orbitals in the range of −6.85 to FL (Fermi level). Moreover, the predominant contribution obtained from the Cl-3s orbital in the range of −14.295 to −12.613 eV has a noticeable contribution from the In-5s and -5p orbitals, and a significant contribution from the Cs-5s orbital occurs in the range of −20.041 to −19.16 eV. The prominent fundamental contribution to the CBM is from the In-5s and In-5p orbitals, with a minor contribution from the Ag-5p and Cs-3p orbitals in the range of 1.9 to 9.1 eV, as shown in Fig. 3b. For CASC, the VBM contributes mainly to the Ag-4d and Cl-3p orbitals, with a

Open Access Article. Published on 07 November 2023. Downloaded on 3/15/2026 12:58:03 PM.
This article is licensed under a Creative Commons Attribution 3.0 Unported Licence.

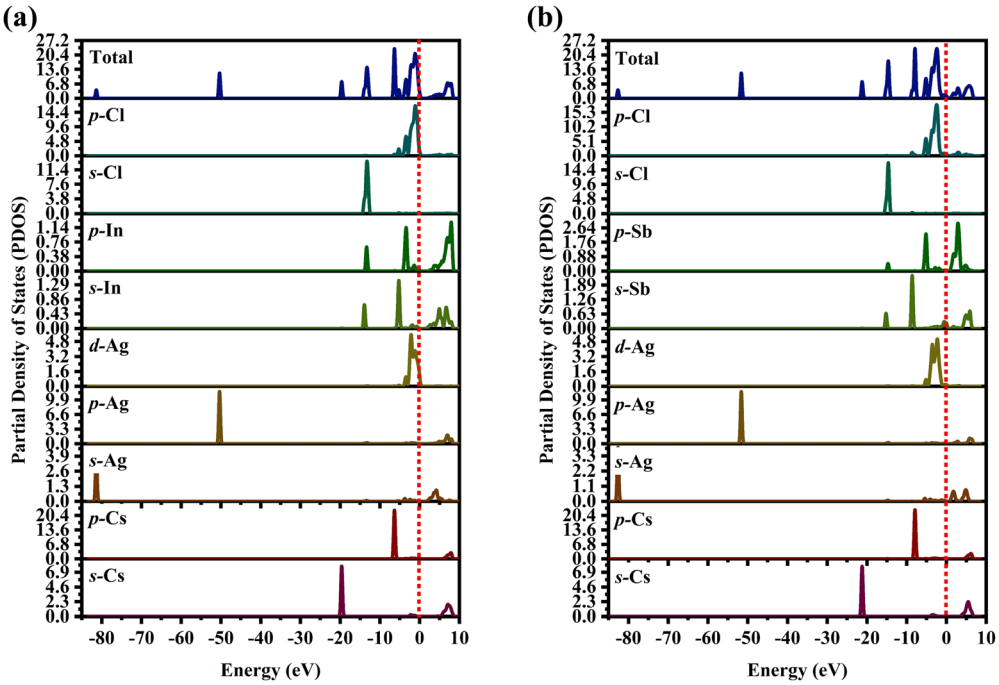

Fig. 4 Partial density of states (PDOS) for (a) CAIC and (b) CASC compounds.

moderate contribution from the Sb-5p orbital in the range of −5.47 to FL. Additionally, the predominant contribution from Cs-5p, Sb-5s, and Sb-5p orbitals ranges from −8.358 to 6.958 eV. Another is the predominant contribution obtained from the Cl-3s orbital in the range of −15.517 to 14.75 eV, with a noticeable contribution from the Sb-5s and Sb-5p orbitals, and a significant contribution from the Cs-5s orbital in the range of −21.67 to −20.752 eV. The prominent fundamental contribution to the CBM is from the Sb-5s and Sb-5p orbitals, with a minor contribution from the Ag-5p and Cs-3p orbitals in the range of 1.1 to 6.5 eV, as shown in Fig. 3d.

The partial density of state PDOS of DP compounds is shown in Fig. 4. The disparity in dispersion between CAIC and CASC compounds comes from the variation in hybridization between Ag-e_g and In/Sb-s states. The lowest portion of the VBM for CAIC and CASC originates from Ag-5s from −82.027 to −80.727 eV, while the middle portion originates from Ag-4p. The CBM originates mostly from the In-5s and -5p orbitals (Fig. 4a) and the Sb-5s and Sb-5p orbitals (Fig. 4b), with minor Ag-5s, Ag-4p, Cs-6s, and Cs-5p orbitals, while the top half of the VBM originates from the Ag-4d, Cs-5p, In-5s, In-5p, Cl-3s, and Cl-3p orbitals. The CBM is mainly derived from the antibonding In-s (Fig. 4a) and Sb-s states (Fig. 4b). Here, we obtain a direct bandgap with the VBM and CBM both at the *G* point for Type-I and an indirect bandgap at the *L*-point for Type-II HDP. Moreover, Ag at the B′-site and Cl at the X-sites are responsible for the electronic structures.

Charge density

According to Han *et al.*,[94] the difference in electron density plays a crucial role in elucidating the bonding characteristics of solid materials from the electron transition, expressed mathematically as $\Delta\rho = \rho A_2B'B''Cl_6 - [\rho A + \rho B' + \rho B'' + \rho Cl]$. The electron localization function (ELF), the HDP density map, and the band-resolved analysis (Fig. 5) elucidate that the electron overlap and the HDP-active electron intensity exhibit a significant concentration that occurs in the region of the distorted $[AgCl_6]^{5-}$ and the antibonding electrons of Cs atoms. The phenomenon of charge transfer in CAIC and CASC compounds

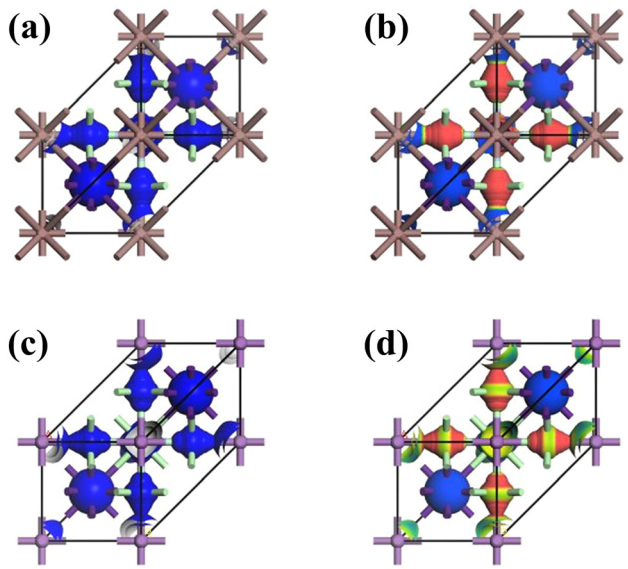

Fig. 5 Electron density map of HDP. (a)–(c) Decreased charge density (initial orbitals-1), and (b)–(d) increased charge density (final orbitals-42) for CAIC and CASC compounds. ELF = 1 (red) and 0 (blue) indicate the accumulated and vanishing electron densities, respectively.

Open Access Article. Published on 07 November 2023. Downloaded on 3/15/2026 12:58:03 PM.
This article is licensed under a Creative Commons Attribution 3.0 Unported Licence.

can be attributed to the collective influence produced by the distorted $[AgCl_6]^{5-}$ units and the emergence of antibonding electrons within cesium (Cs) atoms due to the existence of vacancies. Fig. 5 exhibits the chromatic representation identifying the variation in electron density. The chromatic display of yellow color corresponds to an increase in the spatial distribution of electric charge, while the appearance of blue color corresponds to a decrease in the spatial distribution of electric charge. The analysis of charge transfer in intermolecular and intramolecular systems facilitates prediction of the electronic properties, adsorption behavior, and thermodynamic stability of the mentioned systems. The quantification of the elementary charge of the electron was performed through the utilization of the Mullikan and Hirshfeld methodology, employing the analysis of CAIC and CASC compounds, and the resultant findings are shown in Table 2. The Mullikan population of the alternating corner-shared $[AgCl_6]^{5-}$ octahedrons exhibits a value of 0.41 (CAIC) and 0.26 (CASC), whereas the $[B''Cl_6]^{3-}$ octahedron showcases a value of around 0.18 (CAIC) and 0.13 (CASC).

Optical properties

With the intention to gain insight into the optical characteristics, which hold the greatest importance for the usage of perovskite in optoelectronic devices, an in-depth understanding was achieved by employing the complex dielectric function $\varepsilon(\omega) = \varepsilon_1(\omega) + i\varepsilon_2(\omega)$, as expounded upon in ref. 95 and 96. The frequency-dependent complex dielectric function, $\varepsilon(\omega)$, has been computed, which includes both the real component, $\varepsilon_1(\omega)$, and the imaginary component, $\varepsilon_2(\omega)$. In this investigation, determination of the imaginary component, $\varepsilon_2(\omega)$, was achieved by performing a direct analysis of the electronic structure employing the GGA-PBE method. However, the real component, $\varepsilon_1(\omega)$, was derived through application of the Kramers–Kronig correlation technique, as discussed in ref. 97 and 98. Fig. 6 exhibits the real $[\varepsilon_1(\omega)]$ and imaginary $[\varepsilon_2(\omega)]$ components of the static dielectric function, correspondingly. The real component $[\varepsilon_1(\omega)]$ of the dielectric function serves as an accurate measure of the refractive index. In the field of optical phenomena, it is observed that an enhanced refractive index corresponds to an enhanced probability of light absorption. The imaginary component appears to be the quantum mechanical phenomenon of transitioning from states of occupied bands to states of unoccupied bands. In Fig. 6a–c, we present the electronic contribution within the dielectric function, which has been evaluated employing the GGA-PPE methods. Following this, in Fig. 6c and d, we depict the imaginary part $[\varepsilon_2(\omega)]$ of the dielectric function, which has been determined using the DFPT technique. The measured static values for CAIC and CASC are 3.56 at a wavelength of 277 nm and 5.77 at a wavelength of 841.80 nm, respectively. These values exhibit excellent agreement with previously reported results.[33,60] The theoretical findings reveal an evident difference between the real static value of the CAIC compound and that of the CASC. This difference suggests that the ionic contribution to the dielectric constant is comparatively less significant in the case of CAIC (3.5, at a wavelength of 145.57 nm) in contrast to CASC (3.8, at a wavelength of 346.74 nm), as visually depicted in Fig. 2b–d.

The complex refractive index $m(\lambda)$ can be expressed as a sum of the real part of the refractive index, $m_r(\lambda)$, and the imaginary part, $im_i(\lambda)$, where λ represents the wavelength in free space. The real component of the refractive index can be recognized as the ratio of the velocity of light in a vacuum to the velocity of the phase of an electromagnetic wave propagating through the given medium. The complex component of the refractive index is deeply connected to the absorption coefficient through the expression of $4\pi mi/\lambda$. In the spectrum of refractive indices, exclusively the phenomenon of scattering appears itself. In the category of complex indices, one must recognize the potentiality of both scattering and absorption phenomena. An extensive calculation and comprehensive review of the refractive indices for CAIC and CASC have been undertaken. In Fig. 7, the depicted quantities are the refractive indices, both real and imaginary, related to the materials CAIC and CASC. These indices are presented as functions of wavelength. The theoretical findings reveal that the refractive index, when examined at a wavelength of 263.77 nm, attains its highest value of 1.92 for CAIC (as illustrated in Fig. 7a). Similarly, at a wavelength of 792.597 nm, the refractive indices reach a maximum value of 2.427 for CASC (as depicted in Fig. 7b), which correlates directly with the real component of the dielectric tensor. The observed increase in the CASC can be attributed to the associated decrease in the energy band gap when compared to the CAIC. The refractive index exhibits an increase in value, reaching its maximum at the first transition energy, which corresponds to the electron's leap from the valence band to the conduction band. The observed maxima exhibit an evident shifting towards the lower energy spectrum, thereby signifying an affinity for the transition to appear at lower energy levels. The observed behavior in the case of CASC exhibits abnormalities arising from the associated indirect band gap. In this scenario, a significant abundance of phonon scattering phenomena will appear. The refractive indices of CASIC display significant deviations from those of CAIC for wavelengths exceeding 220 nm (as shown in Fig. 7a–c). The complex refractive indices of both CAIC and CASC exhibit notable absorption features at approximately 137.4 and 141 nm, respectively. It is worth noting that CAIC displays a local minimum in these absorption regions, as depicted in Fig. 7c and d. In contrast, it is observed that CASC exhibits significantly greater

Table 2 Mullikan and Hirshfeld charge analysis of HDP

	CAIC			CASC	
Species ion	Mulliken charge (e)	Hirshfeld charge (e)	Species ion	Mulliken charge (e)	Hirshfeld charge (e)
Cl1	−0.49	−0.18	Cl1	−0.47	−0.18
Cl2	−0.4	−0.18	Cl2	−0.47	−0.18
Cl3	−0.49	−0.18	Cl3	−0.47	−0.18
Cl4	−0.49	−0.18	Cl4	−0.47	−0.18
Cl5	−0.49	−0.18	Cl5	−0.47	−0.18
Cl6	−0.49	−0.18	Cl6	−0.47	−0.18
Ag	0.09	0.30	Ag	—	0.25
In	0.70	0.35	In	0.99	0.41
Cs	1.08	0.21	Cs	0.92	0.21
Cs	1.08	0.21	Cs	0.92	0.21

Open Access Article. Published on 07 November 2023. Downloaded on 3/15/2026 12:58:03 PM.
This article is licensed under a Creative Commons Attribution 3.0 Unported Licence.

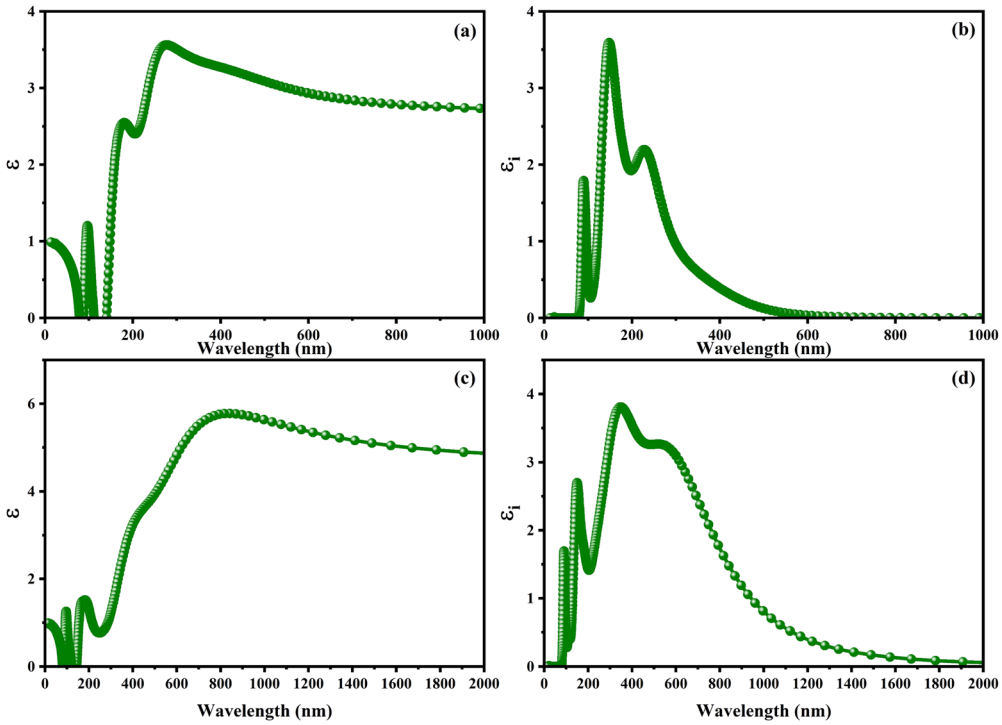

Fig. 6 Optical properties of (a)–(c) real [$\varepsilon_1(\omega)$] and (b)–(d) imaginary [$\varepsilon_2(\omega)$] parts of the static dielectric function for CAIC and CASC compounds.

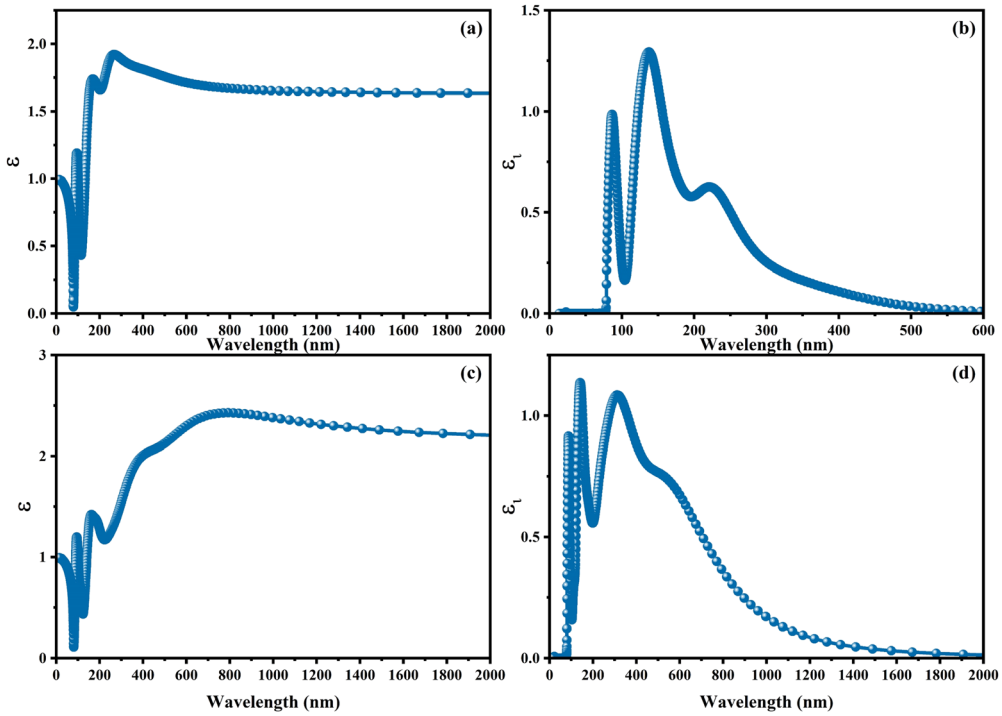

Fig. 7 Optical properties of (a)–(c) real [$m_r(\lambda)$] and (b)–(d) imaginary [$im_i(\lambda)$] parts of the refractive index for CAIC and CASC compounds.

absorption compared to CAIC when considering wavelengths exceeding 195 nm. The refractive indices of CAIC in the UV and visible regions are very small, while they experience a significant increase for CASC, predominantly in the near-infrared region. Based on our analysis, it is inferred that the refractive index of CASC exhibits an enhancement, thereby leading to a corresponding enhancement in its optical characteristics.

Fig. 8 exhibits the absorption spectra, reflectivity, optical conductivity, and loss energy related to the CSIC and CASC compounds. The CSIC and CASC compounds exhibited evident

Open Access Article. Published on 07 November 2023. Downloaded on 3/15/2026 12:58:03 PM.
This article is licensed under a Creative Commons Attribution 3.0 Unported Licence.

absorption, commencing at approximately 78.80 nm, and reaching their peak at 87.14 and 138 nm, respectively. These absorption patterns can be attributed to vibrational phenomena arising from the interplay between B″ and Cl atoms, as visually depicted in Fig. 8a and b. The compound under investigation exhibits an extensive optical absorption phenomenon at wavelengths below 300 nm, while a comparatively weak absorption is observed at 282 nm for CAIC (Fig. 8a). The absorption at 282 nm corresponds to an allowed transition, whereas the absorption at this wavelength is associated with a parity-forbidden transition. The absorption spectra with wavelengths exceeding 400 nm exhibit a direct correlation with the emission of free excitons in the context of CASC compounds, as visually depicted in Fig. 8b. The reflectivity of the CAIC and CASC compounds, when probed at a wavelength of 80.90 nm, has been theoretically determined to be 0.665 and 0.828, respectively. These results suggest a notable degree of reflectivity exhibited by these compounds. The absence of absorption peaks is theoretically detected beyond the 200 nm wavelength for compounds of CASC. However, the observed peaks falling within the wavelength range of 360 to 600 nm can be attributed to the octahedral bonding interactions of $[B''Cl_6]^{3-}$, as visually represented in Fig. 8c and d. At a wavelength of 80.90 nm, most of the detected absorptions are caused by vibrations caused by the interaction between Ag and Cl atomic entities. Fig. 8e and f exhibit the optical conductivity related to the CAIC and CASC compounds. The CAIC successfully exhibits optical conductivity within the wavelength range of 80 to 600 nm, with its peak value reaching 2.99 at 89 nm. Similarly, the CASC demonstrates optical conductivity within the wavelength range of 80 to 1000 nm, with its maximum value recorded as 3.674 at 145.7 nm. These findings are visually represented in Fig. 8f. The depiction of the loss function for CAIC and CASC can be observed in Fig. 8g and h. The observation of energy loss in photoelectrons occurs within the wavelength range of 72 to 84 nm. Particularly, the maximum energy loss value of 66.125 is observed at a wavelength of 78.55 nm for the CAIC system, while the minimum energy loss value of 27.038 is observed at a wavelength of 80.189 nm for the CASC system. These findings are illustrated in Fig. 8g and h.

Phonon vibrational properties

To go deeper into the quantitative understanding of the thermodynamic characteristics resulting from the collective vibrations of atoms within a crystalline structure, our investigation will be directed towards elucidating their temperature-dependent behavior. Phonon oscillation emerges as an essential field within condensed matter systems, with a specific focus on the thermal behavior of solids in correspondence to temperature.[99–103] The thermodynamic metastability of a compound refers to its enthalpy above the ground-state phase(s) under zero pressure and a temperature of 0 K. In the scenario of polymorphs, the compound with the lowest energy and same composition is considered, whereas for materials undergoing phase separation, the energy of the stable decomposition products that are separated by phases is combined in a linear approach. Under situations of applied thermodynamics, such as temperature and pressure variations, the relative stability of different phases may undergo changes. However, it is improbable that the overall

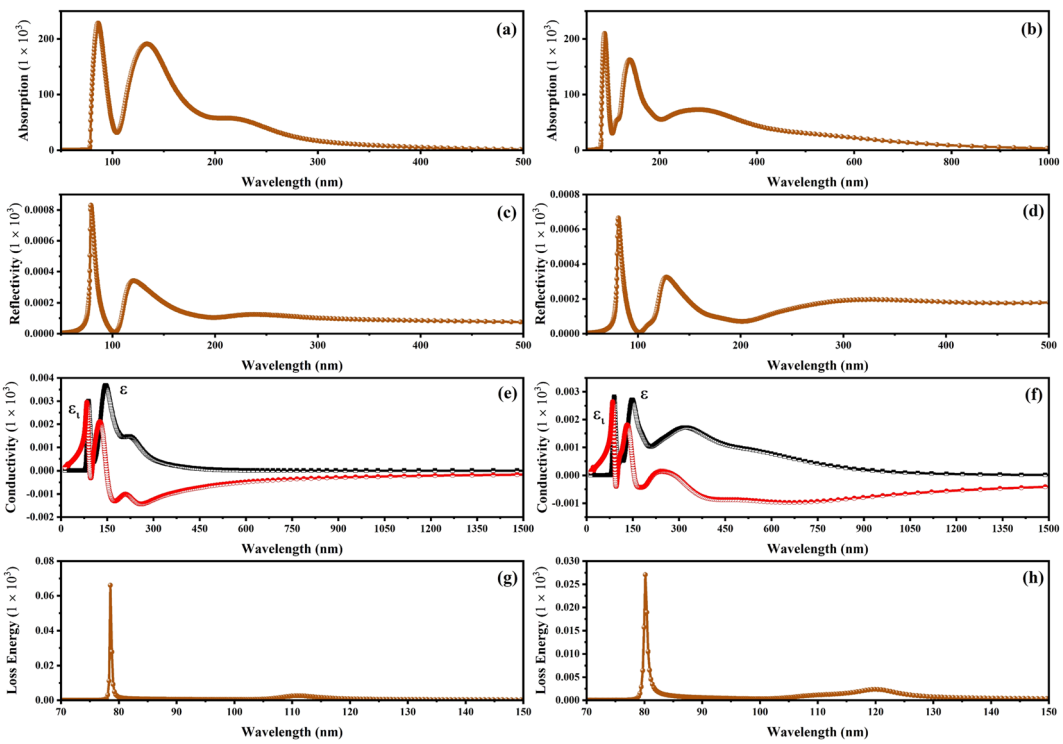

Fig. 8 Other optical properties of CAIC and CASC compounds, including (a) and (b) absorption coefficient, (c) and (d) reflectivity (*R*), (e) and (f) optical conductivity, and (g) and (h) energy loss spectrum using GGA-PBE methods. We used a dividing factor of 1000 to normalize the figures.

 This journal is © the Owner Societies 2023

Open Access Article. Published on 07 November 2023. Downloaded on 3/15/2026 12:58:03 PM.
This article is licensed under a Creative Commons Attribution 3.0 Unported Licence.

thermodynamic scale of metastability deviates much from the one seen at zero temperature and pressure. The greater excess-enthalpy phases are characterized as being "more" metastable, and the concept of metastability is quantified in millielectron volts per atom (10 meV per atom ~1 kJ mol^{-1} atoms), with normalization per atom rather than per formula unit.[104,105] However, the presence of cation defects results in the system transitioning into a state with holes, known as a hole-doped state. On the other hand, the existence of oxygen vacancies creates defect levels that are located close to the lowest energy level of the conduction band. The presence of ordered oxygen vacancies inside HfO layers is thermodynamically advantageous and leads to the development of metallic properties in this system.[106] This phenomenon arises as a result of charge transfer occurring between the vacancy site and the hafnium dangling bond. The electronic properties of Nb- and Tc-doped systems were seen to undergo a transition from insulating to p- and n-type half-metallic ferromagnetic states. One notable aspect of the observation is that oxygen ions exhibit spin polarization, resulting in a magnetic moment of about 0.12 mB per atom. Moreover, these ions play a predominant role in the conductivity of the Nb-doped system.[107]

The determination of the lattice or total energy (E_{tot}) needs a thorough computation of the interplay between electronic and nuclear repulsion through the utilization of first-principles calculations. The evaluation of the relative stability of CAIC and CASC can be achieved through the utilization of entropy, enthalpy, Helmholtz free energy, and specific heat capacity to examine their thermodynamic characteristics. Moreover, the Raman-active modes of the CAIC and CASC systems were computed employing the density functional theory (DFT) approach. The relative stability of the CAIC and CASC can be influenced by the zero-point energies of 0.207 and 0.159 eV, respectively. In Fig. 9, we observe the phonon vibrational and vibrational density of phonon states (VDOS) for the CAIC and CASC systems. The stability of a crystalline structure is ensured when the phonon frequencies of a given unit area show positive values for CAIC and negative values for CASC. This shows that CASC is dynamically unstable. If specific frequencies within a designated spatial region show complex values, commonly known as soft modes, it indicates a state of instability within the system. The evaluation of the phonon density of states is performed using the fundamental principles of phonon theory. This integration is performed within the framework of the quasi-harmonic approximation and can be expressed mathematically using the following equations:

$$F = 3nNk_BT\int_0^{\omega_{max}} \ln\left\{2\sinh\left(\frac{\hbar\omega}{2k_BT}\right)\right\}g(\omega)d\omega \quad (6)$$

$$S = 3nNk_B\int_0^{\omega_{max}} \left(\frac{\hbar\omega}{2k_BT}\right)\coth\left(\frac{\hbar\omega}{2k_BT}\right) - \ln\left\{2\sinh\left(\frac{\hbar\omega}{2k_BT}\right)\right\}g(\omega)d\omega \quad (7)$$

$$C_v = 3nNk_B\int_0^{\omega_{max}} \left(\frac{\hbar\omega}{2k_BT}\right)^2 \mathrm{csch}^2\left(\frac{\hbar\omega}{2k_BT}\right)g(\omega)d\omega \quad (8)$$

Here, the symbol k_B corresponds to the fundamental constant known as the Boltzmann constant. The variable ω_{max} signifies

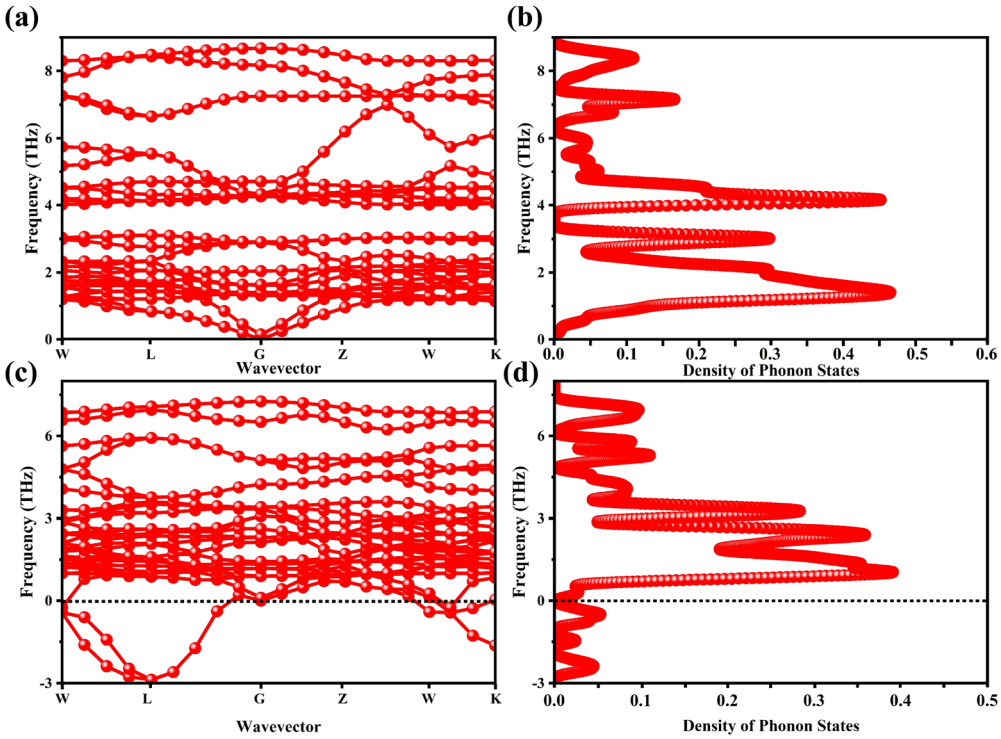

Fig. 9 (a)–(c) Phonon-dispersion curves and (b)–(d) density of phonon states for CAIC and CASC compounds.

Open Access Article. Published on 07 November 2023. Downloaded on 3/15/2026 12:58:03 PM.
This article is licensed under a Creative Commons Attribution 3.0 Unported Licence.

the upper limit of the frequency spectrum associated with phonons. The symbol n represents the quantity of atoms contained within a single unit cell. N, on the other hand, denotes the total number of unit cells present. Lastly, the function $g(\omega)$ characterizes the normalized vibrational density of states (VDOS) with $\int_0^{\omega_{\max}} g(\omega)\mathrm{d}\omega = 1$. The concept of the "quasiharmonic approximation" arises from a methodology in which the evaluation of the Helmholtz free energy, a function dependent on both volume and temperature, is conducted by employing the harmonic approximation for a particular volume. The inclusion of anharmonic contributions is confined to the influence of changes in the system volume on the phonon frequency.

The heat capacity of a substance provides information about vibration properties and energy band structures. To obtain CAIC and CASC, thermodynamic parameters, including the vibrational entropy (E), the vibrational enthalpy (S), the Helmholtz free energy (H), and the specific heat capacity (C_v) at constant volume, have been accurately estimated using the quasi-harmonic approximation method to study the thermodynamic properties of materials. The E, S, H, G, and C_v can be calculated from eqn (6)–(8). Fig. 10 shows the relative thermodynamic parameters of the CAIC and CASC. At 300 K formation, E obtained about 1.48 and 1.54 eV for CAIC and CASC, as shown in Fig. 10a–c. When the temperature is 1000 K, the E increases to 7.853 and 7.79 eV for CAIC and CASC, respectively. The formation of H for CAIC at 300 K is 0.61 eV and is similar to that for CASC. When the temperature increases to 1000 K, the H is 2.39 and 2.29 eV for CAIC and CASC, respectively. The G is about −0.87 and −0.936 eV at 300 K and increases with temperature to obtain −5.47 and −5.67 eV at 1000 K for CAIC and CASC. Fig. 10b–d illustrates a rapid increase in the specific heat capacity (C_v) from 0 to 147 J mol^{-1} K^{-1} as the temperature rises from 0 to 500 K. Fig. 10b–d show the relationship between the heat capacity and temperature (0–1000 K). The results show that the heat capacity of the CAIC and CASC has a similar trend; that is, as the temperature increases, the heat capacity C_v increases. In the temperature range of 0 to 396 K, it is observed that the specific heat capacity of CAIC and CASC exhibits an increasing trend with rising temperature. Furthermore, the slope of the curve undergoes a transition from a relatively large to a small value, indicating a gradual approach towards saturation. Eventually, as the temperature approaches approximately 540 K, the specific heat capacity reaches a constant value. When reflecting specifically on the zero-point energies associated with harmonics, the heat capacity at a constant volume of the CAIC and CASC reaches a limiting value of 57.75 and 55.15 J mol^{-1} K^{-1} at a temperature of 300 K and 59.43 and 56.2 J mol^{-1} K^{-1} at a temperature of 1000 K. Furthermore, it is worth noting that the specific heat capacity values pertaining to CAIC is about 249.3 J mol^{-1} K^{-1}.[108] For the first time, we report the specific heat capacity of CASC.

Using DFT with the GGA and the PBE functional, the Raman active modes of CAIC and CASC were determined. Based on the theoretical framework of group theory, it is anticipated that the cubic phase, which falls under the $Fm\bar{3}m$ (SG: #225, O_h^5) space group, will exhibit four distinct Raman modes denoted as $\Gamma R = 1A_{1g} + E_g + 2T_{2g}$.[27] The atomic distribution corresponding to this configuration can be found in Fig. 11. The cesium (Cs) and chlorine (Cl) atoms can be found occupying the 8c and 24e

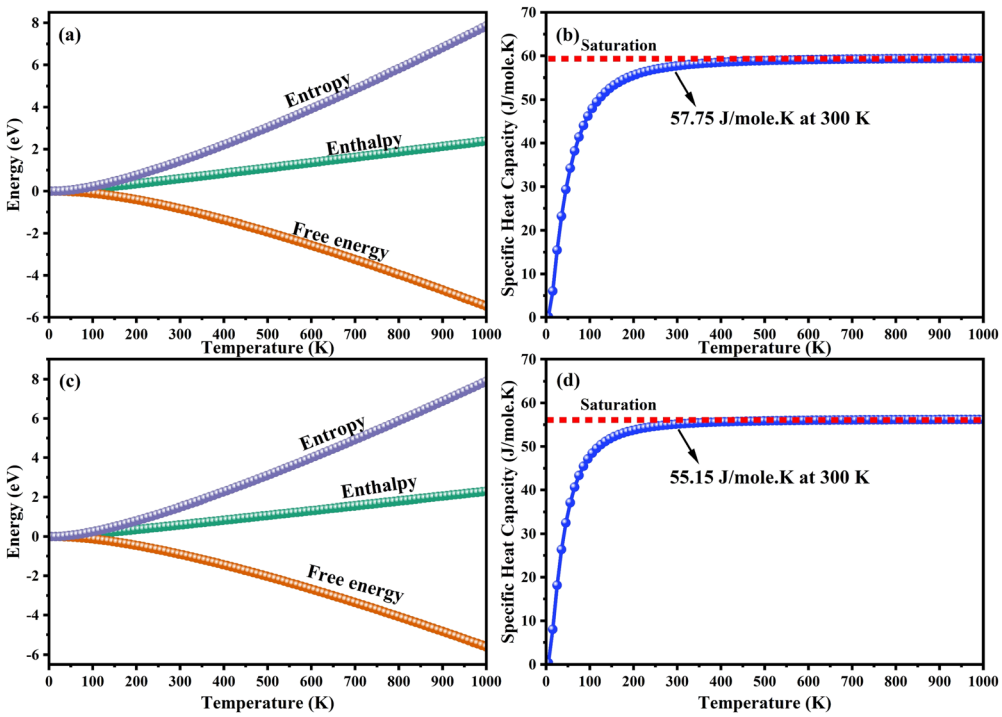

Fig. 10 Temperature dependence of the thermodynamic parameters. (a)–(c) Entropy, enthalpy, free energy and (b)–(d) specific heat capacity at a constant volume of CAIC and CASC compounds.

Open Access Article. Published on 07 November 2023. Downloaded on 3/15/2026 12:58:03 PM.
This article is licensed under a Creative Commons Attribution 3.0 Unported Licence.

Wyckoff sites, respectively. These sites are associated with the indication of Raman activity, characterized by the irreducible representations $1A_{1g}$, E_g, and $2T_{2g}$. The silver (Ag) and indium/antimony (In/Sb) atoms are positioned at the centers of the octahedral units. The local symmetry of this arrangement, known as O_h symmetry, only affects the infrared modes. In terms of irreducible representation, these modes can be described as T_{1u}. The perovskite structure in challenge exhibits a precisely arranged octahedral network composed of [$AgCl_6$] and [$InCl_6$]/[$SbCl_6$] entities, wherein the translational lattice dynamics arise from the Cs–Cl pair bonding interactions. The observed phenomenon can be attributed to the strong presence of lattice modes (specifically, translation and/or libration) involving Cs interacting with Cl and [BCl_6] entities, resulting in low wavenumber vibrations. In the category of high-wavenumber vibrations, the virtual octahedral model emerges as a suitable framework, wherein the internal modes of a single octahedral molecular unit are considered. In this scenario, it is imperative to anticipate the vibrational resonance arising from the molecular ensemble of [$InCl_6$]/[$SbCl_6$], as this particular entity exhibits a stronger bonding characteristic in contrast to [$AgCl_6$]. The presence of silver ions is represented in the vibrational spectrum through the occurrence of rigid displacements of chloride ions.

Yost, Steffens, and Gross have presented the frequencies of the three Raman active modes for a regular octahedral molecule as in the following eqn (9) and (10).[109]

$$\nu_1^2 = (k_{01} + k_{12} + k_{24})/(4\pi^2 m) \quad (9)$$

$$\nu_2^2 = (k_{01} + k_{12} + k_{24} + 3h)/(4\pi^2 m) \quad (10)$$

$$\nu_3^2 = (2k_{12} - 2h)/(4\pi^2 m) \quad (11)$$

In our investigation, we consider the force constants denoted as k_{01}, k_{12}, and k_{24}. These force constants relate to the interactions occurring between the central atom, which can be Ag, In, or Sb in our specific situation, and a peripheral Cl atom. Also, k_{12} stands for the force constant between two neighboring peripheral Cl atoms, while k_{24} stands for the force constant between two diametrically opposite Cl atoms in an octahedral structure, which is shown by $AgCl_6$, $InCl_6$, and $SbCl_6$. The parameter $-h$ quantifies the relative strength of the repulsive interaction generated by two neighboring Cl atoms, with respect to their equilibrium separation. The variable m represents the mass of the peripheral atom Cl. From the eqn (9) and (10), we can observe the presence of the subsequent interrelation.

$$\nu_1^2 = \nu_2^2 + \frac{3}{2}\nu_3^2 \quad (12)$$

In the context of a regular octahedron, the symbols ν_1, ν_2, and ν_3 are representative of the A_{1g}, E_g, and T_{2g} modes, respectively. With the help of *ab initio* calculations, we were able to determine the Raman spectroscopic fingerprint for light with a wavelength of around 520 nm. Through implementing the principles of molecular group theory, we have successfully computed the free vibrations of an isolated octahedral unit composed of [$InCl_6$]/[$SbCl_6$]. The vibrational modes of In/Sb–Cl can be described in terms of their symmetry and corresponding frequencies. The symmetric $A_{1g}(\nu_1)$ mode is observed at 289.49 and 238.98 cm^{-1}. Additionally, the asymmetric $E_g(\nu_2)$ stretchings are found at 144.745 and 170.48 cm^{-1} for CAIC and CASC, respectively. Furthermore, the symmetric $T_{2g}(\nu_5)$ modes are observed in a regular octahedron, as depicted in Fig. 11. The resultant Raman spectrum includes (i) only one lattice motion in the form of a Cs–Cl translation and (ii) a three-part series of internal octahedral vibrations denoted as ν_1, ν_2, and ν_5. The Raman active modes of

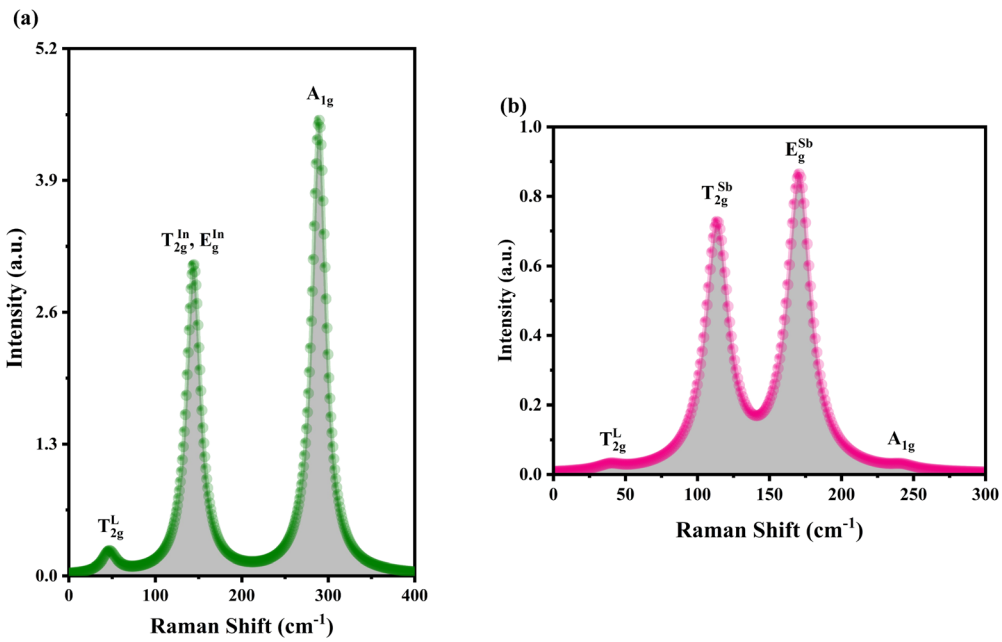

Fig. 11 Calculated Raman active modes at room condition for the ordered cubic (a). CAIC and (b). CASC-compounds.

Open Access Article. Published on 07 November 2023. Downloaded on 3/15/2026 12:58:03 PM.
This article is licensed under a Creative Commons Attribution 3.0 Unported Licence.

Table 3 Calculated Raman active modes under room conditions for the ordered cubic CAIC and CASC and their comparison with experimental data

	CAIC		CASC		
Symmetry	Exp.[110] (cm^{-1})	Our study (cm^{-1})	Exp.[111] (cm^{-1})	Our study (cm^{-1})	Attribute
T_{2g}^{L}	49	46.36	56	40.37	T
$T_{2g}^{B''}$	142	144.76	118	113.28	v_5
$E_{g}^{B''}$	166	144.76	217	170.48	v_2
A_{1g}	300	289.49	288	238.90	v_1

CAIC and CASC, as obtained through experimental measurements and density functional theory (DFT) calculations, are presented in Table 3.

Elastic constants

There is a strong relationship between the elastic constants and the basic properties of the material. This is seen in a wide range of process conditions, such as changes in pressure, temperature, agitation, concentration, and heating. The stiffness matrix C_{ij} of cubic crystals refers to the directional mechanical responses of the indicated crystals to various applied forces. Specifically, the coefficients C_{11}, C_{12}, and C_{44} are intimately linked to this matrix, signifying the distinct mechanical behaviors exhibited by the crystals in response to forces generated in different directions. The longitudinal distortion, denoted as C_{11}, has a complex connection to the longitudinal compression and serves as a fundamental description of the associated hardness. The transverse distortion, denoted as C_{12}, is closely related to the transverse expansion, which in turn is deeply connected to the fundamental concept of Poisson's ratio. The shear elastic parameter, denoted as C_{44}, has a complex connection to the shear modulus, which serves as a fundamental measure of the crystal's rigidity. In the framework of this discussion, it is important to note that Table 4 provides a comprehensive overview of elastic constants for HDP. The values of the bulk modulus (B), shear modulus (G), Young's modulus (E), hardness (H), universal anisotropy index (A^{U}), anisotropy factor in the planes, and Poisson ratio (ν) were obtained *via* rigorous computational analyses. In cubic crystals, the mechanical strength of the crystals is dependent upon the following conditions:

$$C_{44} > 0, \quad C_{11} > C_{12}, \quad C_{11} + 2C_{12} > 0 \qquad (13)$$

The values pertaining to the elastic constants for CAIC and CASC are presented in Table 4. The influence of the B″-site cation on these constants appears as an enhancement of C_{11} across the series ($Cs_2AgSbCl_6$ > $Cs_2AgInCl_6$), which corresponds with the progressive decrease in the ionic radius of the B″ cation. There was a simultaneous decrease in C-12 along the corresponding trajectory. This observation demonstrates that the B″-site induces an apparent effect on the C_{11} parameter in relation to C_{12}. Consequently, the longitudinal compression exhibits progressively greater significance when contrasted with the transverse and shear distortions. Due to the inequality of C_{11} and $C_{12} + 2C_{44}$, an apparent indication of determined longitudinal distortion, particularly in systems incorporating In^+ and Sb^+ ions, it can be inferred that $Cs_2AgB''Cl_6$ (where B″ represents In or Sb) does not exhibit strict isotropy. In accordance with the Voigt–Reuss Hill (VRH) average scheme, the collective bulk modulus (B), shear modulus (G), and Young's modulus (E) can be obtained by considering the elastic constants. The estimated bulk modulus for the CAIC and CASC systems is 22.959 and 22.623 GPa, respectively. The CAIC exhibits a shear modulus of 11.58 GPa, exceeding that of the CSAC, which measures 7.079 GPa. An increased value of the shear modulus signifies an enhanced extent of interatomic bonding. The Young's modulus, denoted by E, and the Poisson ratio, symbolized by ν, are deeply linked to the shear modulus, represented by G, through the equation $E = 9BG/(3B + G)$. Consequently, it is observed that the Young's modulus exhibits a decreasing impact on physical reliability. In contrast to the other HDPs, the CASC material appears to have an exceptionally elevated Poisson's ratio (ν) of 0.358, owing to the tightly arranged atomic lattice within its structure. Moreover, a decrease in the atomic cross-linking degree is observed together with the enhancement of atomic packing, thereby resulting in an elevation of the Poisson ratio. In relation to the field of particle physics, it is observed that the HDP exhibits a lower dimensionality, suggesting the presence of structures with relatively weaker bonds and a more angular nature of these bonds. This is quantified by a ν value of 0.284 for CAIC. In the study conducted by Pugh *et al.*,[112] it was observed that the brittleness of a material presents itself when the ratio of B to G is less than 1.75. Conversely, a material exhibits ductility when the B/G ratio is significantly large. Our investigation has revealed that the CAIC and CASC materials exhibit ductility, characterized by a higher B/G ratio of 1.98 and 3.19, respectively. The utilization of a universal elastic anisotropy index is employed to examine the evolution of microcracks and the fundamental hardness of materials. The CAIC is characterized by an insignificant value of 0.091, in contrast to the CASC, which possesses a more substantial value of 0.468.

Additionally, using the equation, $H = 2(G^3/B^2)^{0.585} - 3$ it is possible to calculate the hardness (H) of HDP in accordance with Chen's proposed formula.[113] Utilizing the prescribed mathematical expression, the value of H has been determined to be 0.762 and −1.384 GPa for the CAIC and CASC compounds, respectively. The use of the shear anisotropic factor technique

Table 4 Elastic constants (GPa), universal anisotropic index, and Poisson ratio of BN polytypes

Compound	B	G	E	H	ν	A^{u}	A_1	A_2	A_3
CAIC	22.968	11.58	29.745	0.762	0.284	0.091	1.8495	1.8495	1.8495
CASC	22.623	7.709	19.23	−1.38	0.358	0.468	1.3166	1.3166	1.3166

Open Access Article. Published on 07 November 2023. Downloaded on 3/15/2026 12:58:03 PM.
This article is licensed under a Creative Commons Attribution 3.0 Unported Licence.

facilitates a greater understanding of the anisotropy associated with the shear modulus across different planes. Based on the discoveries made by Yangthaisong *et al.*,[114] the anisotropic shear factors associated with A_1, A_2, and A_3 can be determined by taking into account the orientations of the shear planes, namely 100, 010, and 001, respectively. These quantities can be determined through the utilization of the subsequent mathematical formulations: $A_1 = 4C_{44}/(C_{11} + C_{33} - 2C_{13})$, $A_2 = 4C_{55}/(C_{22} + C_{33} - 2C_{23})$, and $A_3 = 4C_{66}/(C_{11} + C_{22} - 2C_{12})$, correspondingly. A solid material can be considered isotropic when the values of all its properties exhibit a uniform value of 1. The values of A_1, A_2, and A_3 for the CAIC and CASC systems exhibit values exceeding unity when subjected to atmospheric pressures of 1.849 and 1.316, respectively. Even though the main conditions are the same, the shear anisotropy factors A_1, A_2, and A_3 are not all the same. This is because CAIC and CASC materials are inherently anisotropic. The anisotropic factors exhibit identical characteristics for both the CAIC and CASC compounds.

As part of the Materials Project,[115] the focus is on the 3D analysis and visualization of ELATE, wherein the elastic constants of CAIC and CASC have been employed for the purpose of systematic mechanical characterization. This has been achieved through the utilization of high-throughput calculations pertaining to the elastic constants of inorganic materials, as visually depicted in Fig. 12. The utilization of ELATE (version 2023.01.19, Python 3.10.6), an open-source Python program, is employed for influencing directional elastic characteristics, including the Poisson ratio module, Young's modulus, shear modulus, and spatial dependence on linear compressibility. ELATE provides the second-order elastic constants of C_{ij}s in Voigt notation as a 6 × 6 systematic matrix for the input stiffness matrix (coefficients in GPa) of CAIC and CASC. The construction of the elastic tensor involves the utilization of six eigenvalues. The material exhibits mechanical stability in the presence of positively charged constituents. We observe the physical appearance of Fig. 12(a) and (b), which reveals the complex surface distribution of the elastic modulus of CAIC and CASC, thoroughly portrayed in the three-dimensional (3D) domain. The display of the three-dimensional surface distribution of the blue regions reveals that the anisotropy of the CAIC and CASC increases proportionally with the enhancement of the shear modulus (Fig. 13).

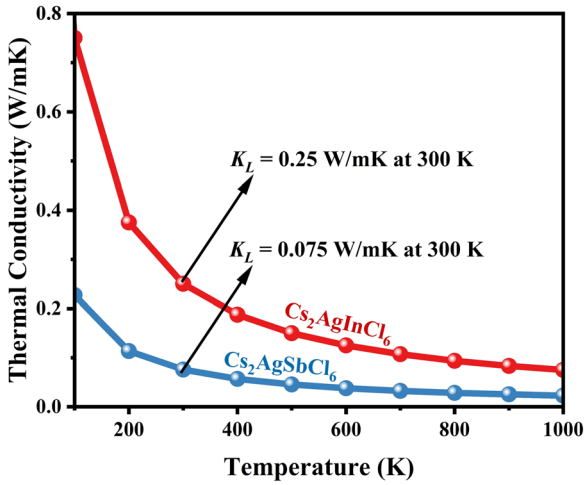

Fig. 13 Calculated ultra-low thermal conductivity of CAIC and CASC compounds *via* temperature. The thermal conductivity decreases as the temperature increases.

Origin of ultra-low thermal conductivity

In the field of thermoelectric applications, the presence of thermal management materials signifies higher efficiency in thermal conductivity, which signifies the capacity to facilitate heat conduction. Materials with high thermal conductivity are employed to optimize the optoelectronic device's performance.

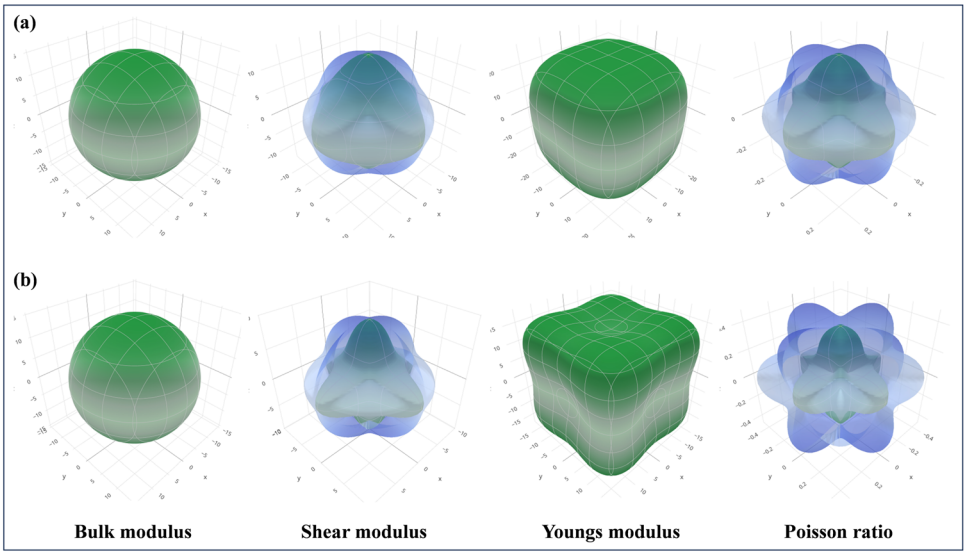

Fig. 12 Spatial dependence of the elastic constants plotted for (a). CAIC and (b). CASC compounds calculated from the online ELATE tool.

Open Access Article. Published on 07 November 2023. Downloaded on 3/15/2026 12:58:03 PM.
This article is licensed under a Creative Commons Attribution 3.0 Unported Licence.

The Debye temperature serves as a fundamental measure of the quantum mechanical interactions governing the cohesive forces exhibited by reactive molecular species.[116–118] Through utilization of the Slack model[119] and the elastic constants (B and G), we can effectively ascertain the Debye temperature and the Grüneisen parameters associated with the acoustic branches. We estimate the thermal conductivity of CAIC and CASC by using the Slack model to calculate the Debye temperature and the Grüneisen parameters of the acoustic branches, which can be accurately determined by the elastic constants (B and G).

$$K_L = A\frac{M_a \delta n^{1/3}\Theta^3}{\gamma_v{}^2 T}, \quad A = \frac{2.43\times10^{-8}}{1-\frac{0.514}{\gamma_v}+\frac{0.228}{\gamma_v{}^2}} \tag{14}$$

Here, $A = \frac{2.43\times10^{-8}}{1-\frac{0.514}{\gamma}+\frac{0.228}{\gamma^2}}$, M_a corresponds to the molar mass, δ corresponds to the volume per atom, n corresponds to the number of atoms, Θ corresponds to the Debye acoustic temperature, γ_v corresponds to the acoustic Grüneisen parameter, k_B corresponds to the Boltzmann constant, N_A corresponds to Avogadro's constant, v_p corresponds to the longitudinal sound velocity, v_s corresponds to the transverse sound velocity, and v_a corresponds to the average sound velocity. To determine Θ, γ_v, v_p, v_s, and v_a the following formulas are used.

$$\Theta = \frac{h}{k_B}\left[\frac{3m}{4\pi}\right]^{1/3} v_a n^{-1/3}, \quad v_a = \left(\frac{1}{3}\left[\frac{1}{v_t{}^3}+\frac{2}{v_l{}^3}\right]\right)^{-1/3} \tag{15}$$

$$v_p = \sqrt{G/\rho}, \quad v_s = \sqrt{(B+4G/3)/\rho} \tag{16}$$

$$\gamma_v = \frac{3}{2}\left(\frac{1+v}{2-3v}\right), \quad v = \frac{1-2(v_t/v_l)^2}{2-2(v_t/v_l)^2} \tag{17}$$

Using eqn (15)–(17), we calculate the Θ, γ_v, v_p, v_s, and v_a. The calculated acoustic Debye temperature is about 183 and 145 K for CAIC and CASC compounds, respectively. The longitudinal velocity is about 3086.2 and 2912.7 m s^{-1}, the transverse velocity is about 1694.8 and 1368.7 m s^{-1}, and the average sound velocity is 2841 and 3583 m s^{-1}, respectively. The significance of ultralow thermal conductivity in materials for thermal management cannot be overemphasized, as it exerts a direct influence on the thermoelectric effect.[120–122] Moreover, optoelectronic devices make use of materials possessing elevated thermal conductivity owing to their capacity to reduce the intrinsic noise emerging from the device.[123] The determination of the thermal conductivity of the CAIC and CASC was achieved through the application of the slack model, as elucidated in eqn (15). The thermal conductivities exhibited by CAIC and CASC materials are approximately 0.075 and 0.25 W m^{-1} K^{-1}, respectively, when subjected to a temperature of 300 K. Moreover, it is important to note that the thermal conductivity values of CAIC and CASC exhibit an enhancement of about 0.41 and 0.5 W m^{-1} K^{-1}, respectively.[103,124] Our findings indicate a reduction in the specific heat capacity by a factor of five, as well as a reduction in the thermal conductivity by a factor of six for CAIC and a factor of two for CASC. The lattice thermal conductivity outcomes of CAIC exhibited an apparent resemblance between $Cs_2BiAgCl_6$ (CABC) and $Cs_2BiAgBr_6$ (CABB), both of which showed remarkably low values at 0.078 and 0.065 W m^{-1} K^{-1}, respectively.[125] These ultra-low thermal conductivity HDP compounds exhibit important properties such as high electrical conductivity, a positive Seebeck coefficient, and an optimal figure of merit. These attributes render them highly suitable for various thermoelectric applications.[126–128]

Conclusions

The analysis of charge transfer in octahedral and intramolecular systems facilitates prediction of the electronic properties, adsorption behavior, and thermodynamic stability of the CAIC and CASC compound and has been been computed by using the density functional theory (DFT) approach. Moreover, the Raman-active modes have been determined using the DFT approach and compared in detail with experimental data. The Raman spectroscopic fingerprint for light with a wavelength of around 520 nm has been obtained *via ab initio* calculations. The entropy, enthalpy, Helmholtz free energy, and specific heat capacity at a constant volume have been accurately estimated using the quasi-harmonic approximation method to study the thermodynamic properties of materials. The thermal conductivities exhibited using CAIC materials are approximately 0.075 and 0.25 W m^{-1} K^{-1}, respectively, when subjected to a temperature of 300 K. The findings from our study indicate a remarkably lowered lattice thermal conductivity. This is due to the low phonon group velocity, low Debye temperature, and large phonon scattering within a large-weighted phase space that contribute to this phenomenon.

Conflicts of interest

The authors declare that they have no known competing financial interests or personal relationships that could appear to influence the work reported in this paper.

Acknowledgements

This research was partially supported by the Grant-in-Aid for Scientific Research No. 21K14510 from the Japan Society for the Promotion of Science (JSPS) and the National Natural Science Foundation of China (No: 62264015 & 22175059). The authors are thankful to Asso. Prof. Raji, Department of Physics, Mepco Schlenk Engineering College, Tamil Nadu, India, for the computational facility.

References

1 S. Chen, H. Yin, P. Liu, Y. Wang and H. Zhao, Stabilization and Performance Enhancement Strategies for Halide Perovskite Photocatalysts, *Adv. Mater.*, 2022, **35**(6), 2203836, DOI: 10.1002/adma.202203836.

Open Access Article. Published on 07 November 2023. Downloaded on 3/15/2026 12:58:03 PM.
This article is licensed under a Creative Commons Attribution 3.0 Unported Licence.

2 J. Li, J. Duan, X. Yang, Y. Duan, P. Yang and Q. Tang, Review on recent progress of lead-free halide perovskites in optoelectronic applications, *Nano Energy*, 2021, **80**, 105526, DOI: 10.1016/j.nanoen.2020.105526.
3 R. Li, H. Jiang, Y. Yao, H. Ye, X. Liu, S. Chen and J. Luo, Bulk Single Crystals of a Narrow Band Gap Three-Dimensional Hybrid Perovskitoid Enabling Ultrastable Photodetection, *Chem. Mater.*, 2022, **34**(23), 10382–10389, DOI: 10.1021/acs.chemmater.2c02109.
4 T. Baikie, Y. Fang, J. M. Kadro, M. Schreyer, F. Wei, S. G. Mhaisalkar, M. Graetzel and T. J. White, Synthesis and crystal chemistry of the hybrid perovskite $(CH_3NH_3)PbI_3$ for solid-state sensitised solar cell applications, *J. Mater. Chem. A*, 2013, **1**(18), 5628, DOI: 10.1039/c3ta10518k.
5 S. D. Stranks and H. J. Snaith, Metal-halide perovskites for photovoltaic and light-emitting devices, *Nat. Nanotechnol.*, 2015, **10**(5), 391–402, DOI: 10.1038/nnano.2015.90.
6 W.-J. Yin, T. Shi and Y. Yan, Superior Photovoltaic Properties of Lead Halide Perovskites: Insights from First-Principles Theory, *J. Phys. Chem. C*, 2015, **119**(10), 5253–5264, DOI: 10.1021/jp512077m.
7 D. Shi, V. Adinolfi, R. Comin, M. Yuan, E. Alarousu, A. Buin, Y. Chen, S. Hoogland, A. Rothenberger, K. Katsiev, Y. Losovyj, X. Zhang, P. A. Dowben, O. F. Mohammed, E. H. Sargent and O. M. Bakr, Low trap-state density and long carrier diffusion in organolead trihalide perovskite single crystals, *Science*, 2015, **347**(6221), 519–522, DOI: 10.1126/science.aaa2725.
8 Z. Guo, Y. Wan, M. Yang, J. Snaider, K. Zhu and L. Huang, Long-range hot-carrier transport in hybrid perovskites visualized by ultrafast microscopy, *Science*, 2017, **356**(6333), 59–62, DOI: 10.1126/science.aam7744.
9 J. M. Ball and A. Petrozza, Defects in perovskite-halides and their effects in solar cells, *Nat. Energy*, 2016, **1**, 16149, DOI: 10.1038/nenergy.2016.149.
10 A. Kojima, K. Teshima, Y. Shirai and T. Miyasaka, Organometal Halide Perovskites as Visible-Light Sensitizers for Photovoltaic Cells, *J. Am. Chem. Soc.*, 2009, **131**(17), 6050–6051, DOI: 10.1021/ja809598r.
11 M. Green, E. Dunlop, J. Hohl-Ebinger, M. Yoshita, N. Kopidakis and X. Hao, Solar cell efficiency tables (version 57), *Prog. Photovoltaics Res. Appl.*, 2020, **29**(1), 3–15, DOI: 10.1002/pip.3371.
12 S. A. Kulkarni, T. Baikie, P. P. Boix, N. Yantara, N. Mathews and S. Mhaisalkar, Band-gap tuning of lead halide perovskites using a sequential deposition process, *J. Mater. Chem. A*, 2014, **2**(24), 9221–9225, DOI: 10.1039/c4ta00435c.
13 A. A. Bakulin, O. Selig, H. J. Bakker, Y. L. A. Rezus, C. Müller, T. Glaser, R. Lovrincic, Z. Sun, Z. Chen, A. Walsh, J. M. Frost and T. L. C. Jansen, Real-Time Observation of Organic Cation Reorientation in Methylammonium Lead Iodide Perovskites, *J. Phys. Chem. Lett.*, 2015, **6**(18), 3663–3669, DOI: 10.1021/acs.jpclett.5b01555.
14 A. R. Srimath Kandada and C. Silva, Exciton Polarons in Two-Dimensional Hybrid Metal-Halide Perovskites, *J. Phys. Chem. Lett.*, 2020, **11**(9), 3173–3184, DOI: 10.1021/acs.jpclett.9b02342.
15 Y. Zhou, L. You, S. Wang, Z. Ku, H. Fan, D. Schmidt, A. Rusydi, L. Chang, L. Wang, P. Ren, L. Chen, G. Yuan, L. Chen and J. Wang, Giant photostriction in organic–inorganic lead halide perovskites, *Nat. Commun.*, 2016, **7**, 11193, DOI: 10.1038/ncomms11193.
16 Z. Song, C. L. McElvany, A. B. Phillips, I. Celik, P. W. Krantz, S. C. Watthage, G. K. Liyanage, D. Apul and M. J. Heben, A technoeconomic analysis of perovskite solar module manufacturing with low-cost materials and techniques, *Energy Environ. Sci.*, 2017, **10**(6), 1297–1305, DOI: 10.1039/c7ee00757d.
17 E. H. Jung, N. J. Jeon, E. Y. Park, C. S. Moon, T. J. Shin, T.-Y. Yang, J. H. Noh and J. Seo, Efficient, stable and scalable perovskite solar cells using poly(3-hexylthiophene, *Nature*, 2019, **567**(7749), 511–515, DOI: 10.1038/s41586-019-1036-3.
18 Q. Jiang, J. Tong, Y. Xian, R. A. Kerner, S. P. Dunfield, C. Xiao, R. A. Scheidt, D. Kuciauskas, X. Wang, M. P. Hautzinger, R. Tirawat, M. C. Beard, D. P. Fenning, J. J. Berry, B. W. Larson, Y. Yan and K. Zhu, Surface reaction for efficient and stable inverted perovskite solar cells, *Nature*, 2022, **611**(7935), 278–283, DOI: 10.1038/s41586-022-05268-x.
19 J. Y. Kim, J.-W. Lee, H. S. Jung, H. Shin and N.-G. Park, High-Efficiency Perovskite Solar Cells, *Chem. Rev.*, 2020, **120**(15), 7867–7918, DOI: 10.1021/acs.chemrev.0c00107.
20 S. Y. Park and K. Zhu, Advances in SnO_2 for Efficient and Stable n–i–p Perovskite Solar Cells, *Adv. Mater.*, 2022, **34**(27), 2110438, DOI: 10.1002/adma.202110438.
21 F. Ünlü, E. Jung, S. Öz, H. Choi, T. Fischer and S. Mathur, *Chemical Processing of Mixed-Cation Hybrid Perovskites: Stabilizing Effects of Configurational Entropy, Perovskite Solar Cells*, Wiley, 2021, pp. 1–31.
22 Z. Ma, X. Ji, S. Lin, X. Chen, D. Wu, X. Li, Y. Zhang, C. Shan, Z. Shi and X. Fang, Recent Advances and Opportunities of Eco-Friendly Ternary Copper Halides: A New Superstar in Optoelectronic Applications, *Adv. Mater.*, 2023, **35**(44), 2300731, DOI: 10.1002/adma.202300731.
23 P. Mandal, B. Show, S. T. Ahmed, D. Banerjee and A. Mondal, Visible-light active electrochemically deposited tin selenide thin films: synthesis, characterization and photocatalytic activity, *J. Mater. Sci.: Mater. Electron.*, 2020, **31**(6), 4708–4718, DOI: 10.1007/s10854-020-03027-0.
24 L. Cheng, D. Li, X. Dong, Q. Ma, W. Yu, J. Wang and G. Liu, A new route to fabricate PbS nanofibers and PbSe nanofibers *via* electrospinning combined with double-crucible technique, *J. Mater. Sci.: Mater. Electron.*, 2016, **27**(9), 9772–9779, DOI: 10.1007/s10854-016-5042-z.
25 A. Maity and B. Ghosh, Fast response paper based visual color change gas sensor for efficient ammonia detection at room temperature, *Sci. Rep.*, 2018, **8**(1), 16851, DOI: 10.1038/s41598-018-33365-3.
26 J.-Y. Lin, J.-H. Liao and T.-C. Wei, Honeycomb-like CoS Counter Electrodes for Transparent Dye-Sensitized Solar Cells, *Electrochem. Solid-State Lett.*, 2011, **14**(4), D41, DOI: 10.1149/1.3533917.
27 H. Ma, C. Li, Y. Ma, H. Wang, Z. W. Rouse, Z. Zhang, C. Slebodnick, A. Alatas, S. P. Baker, J. J. Urban and Z. Tian,

Open Access Article. Published on 07 November 2023. Downloaded on 3/15/2026 12:58:03 PM.
This article is licensed under a Creative Commons Attribution 3.0 Unported Licence.

Supercompliant and Soft $(CH_3NH_3)_3Bi_2I_9$ Crystal with Ultralow Thermal Conductivity, *Phys. Rev. Lett.*, 2019, **123**, 155901, DOI: 10.1103/physrevlett.123.155901.

28 O. Yaffe, Y. Guo, L. Z. Tan, D. A. Egger, T. Hull, C. C. Stoumpos, F. Zheng, T. F. Heinz, L. Kronik, M. G. Kanatzidis, J. S. Owen, A. M. Rappe, M. A. Pimenta and L. E. Brus, Local Polar Fluctuations in Lead Halide Perovskite Crystals, *Phys. Rev. Lett.*, 2017, **118**, 136001, DOI: 10.1103/physrevlett.118.136001.

29 M. A. Haque, S. Kee, D. R. Villalva, W.-L. Ong and D. Baran, Halide Perovskites: Thermal Transport and Prospects for Thermoelectricity, *Adv. Sci.*, 2020, **7**(10), 1903389, DOI: 10.1002/advs.201903389.

30 M. Lai, A. Obliger, D. Lu, C. S. Kley, C. G. Bischak, Q. Kong, T. Lei, L. Dou, N. S. Ginsberg, D. T. Limmer and P. Yang, Intrinsic anion diffusivity in lead halide perovskites is facilitated by a soft lattice, *Proc. Natl. Acad. Sci. U. S. A.*, 2018, **115**(47), 11929–11934, DOI: 10.1073/pnas.1812718115.

31 Z. Xiao, Y. Yuan, Y. Shao, Q. Wang, Q. Dong, C. Bi, P. Sharma, A. Gruverman and J. Huang, Giant switchable photovoltaic effect in organometal trihalide perovskite devices, *Nat. Mater.*, 2014, **14**(2), 193–198, DOI: 10.1038/nmat4150.

32 G. Y. Kim, A. Senocrate, T.-Y. Yang, G. Gregori, M. Grätzel and J. Maier, Large tunable photoeffect on ion conduction in halide perovskites and implications for photodecomposition, *Nat. Mater.*, 2018, **17**(5), 445–449, DOI: 10.1038/s41563-018-0038-0.

33 Y. Yuan and J. Huang, Ion Migration in Organometal Trihalide Perovskite and Its Impact on Photovoltaic Efficiency and Stability, *Acc. Chem. Res.*, 2016, **49**(2), 286–293, DOI: 10.1021/acs.accounts.5b00420.

34 E. Bi, Z. Song, C. Li, Z. Wu and Y. Yan, Mitigating ion migration in perovskite solar cells, *Trends Chem.*, 2021, **3**(7), 575–588, DOI: 10.1016/j.trechm.2021.04.004.

35 Y.-C. Zhao, W.-K. Zhou, X. Zhou, K.-H. Liu, D.-P. Yu and Q. Zhao, Quantification of light-enhanced ionic transport in lead iodide perovskite thin films and its solar cell applications, *Light: Sci. Appl.*, 2017, **6**(5), e16243, DOI: 10.1038/lsa.2016.243.

36 E. Shirzadi, N. Tappy, F. Ansari, M. K. Nazeeruddin, A. Hagfeldt and P. J. Dyson, Deconvolution of Light-Induced Ion Migration Phenomena by Statistical Analysis of Cathodoluminescence in Lead Halide-Based Perovskites, *Adv. Sci.*, 2022, **9**(13), e2103729, DOI: 10.1002/advs.202103729.

37 J. Barbé, M. Newman, S. Lilliu, V. Kumar, H. K. H. Lee, C. Charbonneau, C. Rodenburg, D. Lidzey and W. C. Tsoi, Localized effect of PbI2 excess in perovskite solar cells probed by high-resolution chemical–optoelectronic mapping, *J. Mater. Chem. A*, 2018, **6**(45), 23010–23018, DOI: 10.1039/c8ta09536a.

38 D. W. deQuilettes, W. Zhang, V. M. Burlakov, D. J. Graham, T. Leijtens, A. Osherov, V. Bulović, H. J. Snaith, D. S. Ginger and S. D. Stranks, Photo-induced halide redistribution in organic-inorganic perovskite films, *Nat. Commun.*, 2016, **7**, 11683, DOI: 10.1038/ncomms11683.

39 Y. Yuan, Q. Wang, Y. Shao, H. Lu, T. Li, A. Gruverman and J. Huang, Electric-Field-Driven Reversible Conversion Between Methylammonium Lead Triiodide Perovskites and Lead Iodide at Elevated Temperatures, *Adv. Energy Mater.*, 2015, **6**(2), 1501803, DOI: 10.1002/aenm.201501803.

40 N. P. Mathew, N. R. Kumar and R. Radhakrishnan, First Principle Study of the Structural and Optoelectronic Properties of Direct Bandgap Double Perovskite $Cs_2AgInCl_6$, *Mater. Today: Proc.*, 2020, **33**, 1252–1256, DOI: 10.1016/j.matpr.2020.03.489.

41 F. Igbari, F.-F. Xu, J.-Y. Shao, F. Ud-Din, P. Siffalovic and Y.-W. Zhong, Stacking Interactions and Photovoltaic Performance of Cs2AgBiBr6 Perovskite, *Sol. RRL*, 2023, **7**, 2200932, DOI: 10.1002/solr.202200932.

42 Y. Ye, Y. Yin, Y. Chen, S. Li, L. Li and Y. Yamauchi, Metal-Organic Framework Materials in Perovskite Solar Cells: Recent Advancements and Perspectives, *Small*, 2023, **19**(25), 2208119, DOI: 10.1002/smll.202208119.

43 Y. Wu, X. Li and H. Zeng, Lead-Free Halide Double Perovskites: Structure, Luminescence, and Applications, *Small Struct.*, 2020, **2**(3), 2000071, DOI: 10.1002/sstr.202000071.

44 L. Lu, X. Pan, J. Luo and Z. Sun, Recent Advances and Optoelectronic Applications of Lead-Free Halide Double Perovskites, *Chem. – Eur. J.*, 2020, **26**(71), 16975–16984, DOI: 10.1002/chem.202000788.

45 F. Ji, G. Boschloo, F. Wang and F. Gao, Challenges and Progress in Lead-Free Halide Double Perovskite Solar Cells, *Sol. RRL*, 2023, **7**(6), 2201112, DOI: 10.1002/solr.202201112.

46 H. Tang, Y. Xu, X. Hu, Q. Hu, T. Chen, W. Jiang, L. Wang and W. Jiang, Lead-Free Halide Double Perovskite Nanocrystals for Light-Emitting Applications: Strategies for Boosting Efficiency and Stability, *Adv. Sci.*, 2021, **8**(7), 2004118, DOI: 10.1002/advs.202004118.

47 S. Chand Yadav, A. Srivastava, V. Manjunath, A. Kanwade, R. S. Devan and P. M. Shirage, Properties, performance and multidimensional applications of stable lead-free $Cs_2AgBiBr_6$ double perovskite, *Mater. Today Phys.*, 2022, **26**, 100731, DOI: 10.1016/j.mtphys.2022.100731.

48 J. Wang, L. Wang, F. Wang, S. Jiang and H. Guo, Pressure-induced bandgap engineering of lead-free halide double perovskite $(NH_4)_2SnBr_6$, *Phys. Chem. Chem. Phys.*, 2021, **23**(35), 19308–19312, DOI: 10.1039/d1cp03267d.

49 M. L. Zaffalon, F. Cova, M. Liu, A. Cemmi, I. Di Sarcina, F. Rossi, F. Carulli, A. Erroi, C. Rodà, J. Perego, A. Comotti, M. Fasoli, F. Meinardi, L. Li, A. Vedda and S. Brovelli, Extreme γ-ray radiation hardness and high scintillation yield in perovskite nanocrystals, *Nat. Photonics*, 2022, **16**(12), 860–868, DOI: 10.1038/s41566-022-01103-x.

50 Y. Bai, M. Hao, S. Ding, P. Chen and L. Wang, Surface Chemistry Engineering of Perovskite Quantum Dots: Strategies, Applications, and Perspectives, *Adv. Mater.*, 2021, **34**(4), 2105958, DOI: 10.1002/adma.202105958.

51 T. Yang, F. Li and R. Zheng, Recent advances in radiation detection technologies enabled by metal-halide perovskites, *Mater. Adv.*, 2021, **2**(21), 6744–6767, DOI: 10.1039/d1ma00569c.

52 K. Sakhatskyi, B. Turedi, G. J. Matt, E. Wu, A. Sakhatska, V. Bartosh, M. N. Lintangpradipto, R. Naphade, I. Shorubalko,

 This journal is © the Owner Societies 2023

Open Access Article. Published on 07 November 2023. Downloaded on 3/15/2026 12:58:03 PM.
This article is licensed under a Creative Commons Attribution 3.0 Unported Licence.

O. F. Mohammed, S. Yakunin, O. M. Bakr and M. V. Kovalenko, Stable perovskite single-crystal X-ray imaging detectors with single-photon sensitivity, *Nat. Photonics*, 2023, **17**(6), 510–517, DOI: 10.1038/s41566-023-01207-y.

53 W. Guo, X. Liu, S. Han, Y. Liu, Z. Xu, M. Hong, J. Luo and Z. Sun, Room-Temperature Ferroelectric Material Composed of a Two-Dimensional Metal Halide Double Perovskite for X-ray Detection, *Angew. Chem., Int. Ed.*, 2020, **59**(33), 13879–13884, DOI: 10.1002/anie.202004235.

54 Y. Liu, Y. Jing, J. Zhao, Q. Liu and Z. Xia, Design Optimization of Lead-Free Perovskite $Cs_2AgInCl_6$:Bi Nanocrystals with 11.4% Photoluminescence Quantum Yield, *Chem. Mater.*, 2019, **31**(9), 3333–3339, DOI: 10.1021/acs.chemmater.9b00410.

55 Y. Fang, L. Zhang, L. Sui, J. Yan, K. Wang, K. Yuan, W. L. Mao and B. Zou, Tuning Emission and Electron-Phonon Coupling in Lead-Free Halide Double Perovskite $Cs_2AgBiCl_6$ under Pressure, *ACS Energy Letters*, 2019, **4**(12), 2975–2982, DOI: 10.1021/acsenergylett.9b02155.s001.

56 B. Ke, R. Zeng, Z. Zhao, Q. Wei, X. Xue, K. Bai, C. Cai, W. Zhou, Z. Xia and B. Zou, Homo- and Heterovalent Doping-Mediated Self-Trapped Exciton Emission and Energy Transfer in Mn-Doped $Cs_2Na_{1-x}AgxBiCl_6$ Double Perovskites, *J. Phys. Chem. Lett.*, 2019, **11**(1), 340–348, DOI: 10.1021/acs.jpclett.9b03387.

57 T. T. Tran, J. R. Panella, J. R. Chamorro, J. R. Morey and T. M. McQueen, Designing indirect–direct bandgap transitions in double perovskites, *Mater. Horiz.*, 2017, **4**(4), 688–693, DOI: 10.1039/c7mh00239d.

58 P. Xu, H. Ye, Y. Yao, T. Zhu and J. Luo, Lead-Free Double Perovskite Semiconductor with Rigid Spacer-Induced High-Tc Dielectric Switch Features, *Chem. – Eur. J.*, 2023, **29**(40), e202300667, DOI: 10.1002/chem.202300667.

59 M. S. Shadabroo, H. Abdizadeh and M. R. Golobostanfard, Elpasolite structures based on A_2AgBiX_6 (A: MA, Cs, X: I, Br): Application in double perovskite solar cells, *Mater. Sci. Semicond. Process.*, 2021, **125**, 105639, DOI: 10.1016/j.mssp.2020.105639.

60 C. Dong, X. Guan, Z. Wang, H. Zhao, Y. Kuai, S. Gao, C. Chen, W. Zou and P. Lu, The effects of cation and halide anion on the stability, electronic and optical properties of double perovskite Cs_2NaMX_6 (M = In, Tl, Sb, bi; X = Cl, Br, I), *Comput. Mater. Sci.*, 2023, **220**, 112058, DOI: 10.1016/j.commatsci.2023.112058.

61 W. Li, Y. Li, Z. Zhang and P. Gao, Alternative lead-free mixed-valence double perovskites for high-efficiency photovoltaic applications, *J. Energy Chem.*, 2023, **84**, 347–353, DOI: 10.1016/j.jechem.2023.05.037.

62 P. E. Blöchl, Projector augmented-wave method, *Phys. Rev. B: Condens. Matter Mater. Phys.*, 1994, **50**(24), 17953–17979, DOI: 10.1103/physrevb.50.17953.

63 V. Milman, K. Refson, S. J. Clark, C. J. Pickard, J. R. Yates, S. P. Gao, P. J. Hasnip, M. I. J. Probert, A. Perlov and M. D. Segall, Electron and vibrational spectroscopies using DFT, plane waves and pseudopotentials: CASTEP implementation, *THEOCHEM*, 2010, **954**(1–3), 22–35, DOI: 10.1016/j.theochem.2009.12.040.

64 P.-O. Löwdin, Quantum theory of cohesive properties of solids, *Adv. Phys.*, 2001, **50**(6), 597–756, DOI: 10.1080/00018730110102196.

65 Y. Jiang and Z. Miao, Quasi-Newton Waveform Relaxation Based on Energy Method, *J. Comput. Math.*, 2018, **36**(4), 542–562, DOI: 10.4208/jcm.1702-m2016-0700.

66 H. J. Monkhorst and J. D. Pack, Special points for Brillouin-zone integrations, *Phys. Rev. B: Solid State*, 1976, **13**(12), 5188–5192, DOI: 10.1103/physrevb.13.5188.

67 J. Zhou, X. Rong, M. S. Molokeev, X. Zhang and Z. Xia, Exploring the transposition effects on the electronic and optical properties of $Cs_2AgSbCl_6$ *via* a combined computational-experimental approach, *J. Mater. Chem. A*, 2018, **6**(5), 2346–2352, DOI: 10.1039/c7ta10062k.

68 L. Katz and R. Ward, Structure Relations in Mixed Metal Oxides, *Inorg. Chem.*, 1964, **3**(2), 205–211, DOI: 10.1021/ic50012a013.

69 M. W. Lufaso and P. M. Woodward, *Using Bond Valences to Model the Structures of Ternary and Quaternary Oxides, Structure and Bonding*, Springer Berlin Heidelberg, 2013, pp. 59–90.

70 I. D. Brown and D. Altermatt, Bond-valence parameters obtained from a systematic analysis of the Inorganic Crystal Structure Database, *Acta Crystallogr., Sect. B: Struct. Sci.*, 1985, **41**(4), 244–247, DOI: 10.1107/s0108768185002063.

71 C. Sun, J. A. Alonso and J. Bian, Recent Advances in Perovskite-Type Oxides for Energy Conversion and Storage Applications, *Adv. Energy Mater.*, 2020, **11**(2), 2000459, DOI: 10.1002/aenm.202000459.

72 C. A. López, M. C. Alvarez-Galván, M. V. Martínez-Huerta, F. Fauth and J. A. Alonso, Crystal structure features of $CH_3NH_3PbI_{3-x}Br_x$ hybrid perovskites prepared by ball milling: a route to more stable materials, *CrystEngComm*, 2020, **22**(4), 767–775, DOI: 10.1039/c9ce01461f.

73 C. A. López, C. Abia, M. C. Alvarez-Galván, B.-K. Hong, M. V. Martínez-Huerta, F. Serrano-Sánchez, F. Carrascoso, A. Castellanos-Gómez, M. T. Fernández-Díaz and J. A. Alonso, Crystal Structure Features of $CsPbBr_3$ Perovskite Prepared by Mechanochemical Synthesis, *ACS Omega*, 2020, **5**(11), 5931–5938, DOI: 10.1021/acsomega.9b04248.

74 X. Zhao, Q. Guo, B. Song, J. Luo and J. Tang, Light Emission of Self-Trapped Excitons in Inorganic Metal Halides for Optoelectronic Applications, *Adv. Mater.*, 2022, **34**(52), 2201008, DOI: 10.1002/adma.202201008.

75 Q. A. Akkerman and L. Manna, What Defines a Halide Perovskite?, *ACS Energy Lett.*, 2020, **5**(2), 604–610, DOI: 10.1021/acsenergylett.0c00039.

76 N. Mercier, Hybrid Halide Perovskites: Discussions on Terminology and Materials, *Angew. Chem., Int. Ed.*, 2019, **58**(50), 17912–17917, DOI: 10.1002/anie.201909601.

77 D. Prasad and N. Mitra, Catalytic Behavior of Hydrogen Bonded Water in Oligomerization of Silicates, *Inorg. Chem.*, 2023, **62**(4), 1423–1436, DOI: 10.1021/acs.inorgchem.2c03509.

78 R. D. Shannon, Revised effective ionic radii and systematic studies of interatomic distances in halides and chalcogenides, *Acta Crystallogr., Sect. A: Cryst. Phys., Diffr., Theor.*

Open Access Article. Published on 07 November 2023. Downloaded on 3/15/2026 12:58:03 PM.
This article is licensed under a Creative Commons Attribution 3.0 Unported Licence.

Gen. Crystallogr., 1976, **32**(5), 751–767, DOI: 10.1107/s0567739476001551.

79 P. G. Radaelli, G. Iannone, M. Marezio, H. Y. Hwang, S. W. Cheong, J. D. Jorgensen and D. N. Argyriou, Structural Effects on the Magnetic and Transport Properties of Perovskite $A_{1-x}A_x'MnO_3$ (x = 0.25, 0.30), *Phys. Rev. B: Condens. Matter Mater. Phys.*, 1997, **56**(13), 8265–8276, DOI: 10.1103/physrevb.56.8265.

80 B. Yang, X. Mao, F. Hong, W. Meng, Y. Tang, X. Xia, S. Yang, W. Deng and K. Han, Lead-Free Direct Band Gap Double-Perovskite Nanocrystals with Bright Dual-Color Emission, *J. Am. Chem. Soc.*, 2018, **140**(49), 17001–17006, DOI: 10.1021/jacs.8b07424.

81 A. A. Haghighirad, G. Volonakis, R. L. Milot, W. H. Sio, M. R. Filip, B. Wenger, M. B. Johnston, L. M. Herz, H. J. Snaith and F. Giustino, $Cs_2InAgCl_6$: A New Lead-Free Halide Double Perovskite with Direct Band Gap, *J. Phys. Chem. Lett*, 2017, **8**(4), 772–778, DOI: 10.1021/acs.jpclett.6b02682.

82 J. Luo, S. Li, H. Wu, Y. Zhou, Y. Li, J. Liu, J. Li, K. Li, F. Yi, G. Niu and J. Tang, $Cs_2AgInCl_6$ Double Perovskite Single Crystals: Parity Forbidden Transitions and Their Application For Sensitive and Fast UV Photodetectors, *ACS Photonics*, 2018, **5**(2), 398–405, DOI: 10.1021/acsphotonics.7b00837.

83 K. Nila Nandha and A. Nag, Synthesis and luminescence of Mn-doped $Cs_2AgInCl_6$ double perovskites, *Chem. Commun.*, 2018, **54**(41), 5205–5208, DOI: 10.1039/c8cc01982g.

84 J. Zhou, Z. Xia, M. S. Molokeev, X. Zhang, D. Peng and Q. Liu, Composition design, optical gap and stability investigations of lead-free halide double perovskite $Cs_2AgInCl_6$, *J. Mater. Chem. A*, 2017, **5**(29), 15031–15037, DOI: 10.1039/c7ta04690a.

85 A. Karmakar, G. M. Bernard, A. Meldrum, A. O. Oliynyk and V. K. Michaelis, Tailorable Indirect to Direct Band-Gap Double Perovskites with Bright White-Light Emission: Decoding Chemical Structure Using Solid-State NMR, *J. Am. Chem. Soc.*, 2020, **142**(24), 10780–10793, DOI: 10.1021/jacs.0c02198.

86 D. Manna, J. Kangsabanik, T. K. Das, D. Das, A. Alam and A. Yella, Lattice Dynamics and Electron–Phonon Coupling in Lead-Free $Cs_2AgIn_{1-x}Bi_xCl_6$ Double Perovskite Nanocrystals, *J. Phys. Chem. Lett.*, 2020, **11**(6), 2113–2120, DOI: 10.1021/acs.jpclett.0c00206.

87 T. Appadurai, R. Kashikar, P. Sikarwar, S. Antharjanam, B. R. K. Nanda and A. K. Chandiran, Manipulation of parity and polarization through structural distortion in light-emitting halide double perovskites, *Commun. Mater.*, 2021, **2**, 68, DOI: 10.1038/s43246-021-00172-9.

88 J. Luo, X. Wang, S. Li, J. Liu, Y. Guo, G. Niu, L. Yao, Y. Fu, L. Gao, Q. Dong, C. Zhao, M. Leng, F. Ma, W. Liang, L. Wang, S. Jin, J. Han, L. Zhang, J. Etheridge, J. Wang, Y. Yan, E. H. Sargent and J. Tang, Efficient and stable emission of warm-white light from lead-free halide double perovskites, *Nature*, 2018, **563**(7732), 541–545, DOI: 10.1038/s41586-018-0691-0.

89 Y. Liu, M. S. Molokeev and Z. Xia, Lattice Doping of Lanthanide Ions in $Cs_2AgInCl_6$ Nanocrystals Enabling Tunable Photoluminescence, *Energy Mater. Adv.*, 2021, **2021**, 2585274, DOI: 10.34133/2021/2585274.

90 R. Singh Lamba, P. Basera, S. Singh, S. Bhattacharya and S. Sapra, Lead-Free Alloyed Double-Perovskite Nanocrystals of $Cs_2(Na_xAg_{1-x})BiBr_6$ with Tunable Band Gap, *J. Phys. Chem. C*, 2021, **125**(3), 1954–1962, DOI: 10.1021/acs.jpcc.0c09554.s001.

91 R. S. Lamba, P. Basera, S. Bhattacharya and S. Sapra, Band Gap Engineering in $Cs_2(NaxAg_{1-x})BiCl_6$ Double Perovskite Nanocrystals, *J. Phys. Chem. Lett.*, 2019, **10**(17), 5173–5181, DOI: 10.1021/acs.jpclett.9b02168.

92 D. Tu, Y. Pei, C. Li, S. Han, Z. Xie, F. Wen, L. Wang and X. Chen, Boosting Near-Infrared Luminescence of Lanthanide in $Cs_2AgBiCl_6$ Double Perovskites *via* Breakdown of the Local Site Symmetry, *Angew. Chem., Int. Ed.*, 2022, **61**(30), e202205276, DOI: 10.1002/anie.202205276.

93 D. Gill, P. Bhumla, M. Kumar and S. Bhattacharya, High-throughput screening to modulate electronic and optical properties of alloyed $Cs_2AgBiCl_6$ for enhanced solar cell efficiency, *J. Phys.: Mater.*, 2021, **4**(2), 025005, DOI: 10.1088/2515-7639/abe7d6.

94 X. Han, J. Lin, J. Liu, N. Wang and D. Pan, Effects of Hexagonal Boron Nitride Encapsulation on the Electronic Structure of Few-Layer MoS_2, *J. Phys. Chem. C*, 2019, **123**(23), 14797–14802, DOI: 10.1021/acs.jpcc.9b02549.

95 J. S. Toll, Causality and the Dispersion Relation: Logical Foundations, *Phys. Rev.*, 1956, **104**(6), 1760–1770, DOI: 10.1103/physrev.104.1760.

96 S. Saha, T. P. Sinha and A. Mookerjee, Electronic Structure, Chemical Bonding, and Optical Properties of paraelectric BaTiO, *Phys. Rev. B: Condens. Matter Mater. Phys.*, 2000, **62**(13), 8828–8834, DOI: 10.1103/physrevb.62.8828.

97 V. Kumar and R. Santosh, *The Stability, Structural, Electronic, and Optical Properties of Hydrogenated Silicene Under Hydrostatic Pressures: A First-principle Study*, Research Square Platform LLC, 2021.

98 J. Xiao, Z. He, S. Zhu, B. Chen and G. Jiang, Hybrid functional study of structural, electronic, bonding and optical properties of $CdSiP_2$, *Comput. Mater. Sci.*, 2016, **117**, 472–477, DOI: 10.1016/j.commatsci.2016.02.014.

99 D. C. Wallace and H. Callen, Thermodynamics of Crystals, *Am. J. Phys.*, 1972, **40**(11), 1718–1719, DOI: 10.1119/1.1987046.

100 W. Cochran and R. A. Cowley, Dielectric constants and lattice vibrations, *J. Phys. Chem. Solids*, 1962, **23**(5), 447–450, DOI: 10.1016/0022-3697(62)90084-7.

101 A. J. C. Wilson, Dynamical Theory of Crystal Lattices by M. Born and K. Huang, *Acta Crystallogr.*, 1955, **8**(7), 444, DOI: 10.1107/s0365110x5500279x.

102 K. Refson, P. R. Tulip and S. J. Clark, Variational density-functional perturbation theory for dielectrics and lattice dynamics, *Phys. Rev. B: Condens. Matter Mater. Phys.*, 2006, **73**, 155114, DOI: 10.1103/physrevb.73.155114.

103 J. Su, Z. Zhang, J. Hou, M. Liu, Z. Lin, Z. Hu, J. Chang and Y. Hao, Pressure-Dependent Mechanical and Thermal Properties of Lead-Free Halide Double Perovskite $Cs_2AgB''X_6$

Open Access Article. Published on 07 November 2023. Downloaded on 3/15/2026 12:58:03 PM.
This article is licensed under a Creative Commons Attribution 3.0 Unported Licence.

(B″ = In, Bi; X = Cl, Br, I), *Adv. Theory Simul.*, 2019, **2**(12), 1900164, DOI: 10.1002/adts.201900164.

104 W. Sun, S. T. Dacek, S. P. Ong, G. Hautier, A. Jain, W. D. Richards, A. C. Gamst, K. A. Persson and G. Ceder, The thermodynamic scale of inorganic crystalline metastability, *Sci. Adv.*, 2016, **2**(11), e1600225, DOI: 10.1126/sciadv.1600225.

105 S. Kirklin, J. E. Saal, B. Meredig, A. Thompson, J. W. Doak, M. Aykol, S. Rühl and C. Wolverton, The Open Quantum Materials Database (OQMD): assessing the accuracy of DFT formation energies, *npj Comput. Mater.*, 2015, **1**(1), 1–5, DOI: 10.1038/npjcompumats.2015.10.

106 S. M. Alay-e-Abbas, S. Nazir, N. A. Noor, N. Amin and A. Shaukat, Thermodynamic stability and vacancy defect formation energies in $SrHfO_3$, *J. Phys. Chem. C*, 2014, **118**(34), 19625–19634, DOI: 10.1021/jp506263g.

107 S. Faiza-Rubab, S. Naseem, S. M. Alay-e-Abbas, M. Zulfiqar, Y. Zhao and S. Nazir, Structural stability and evolution of half-metallicity in Ba_2CaMoO_6: interplay of hole-and electron-doping, *Phys. Chem. Chem. Phys.*, 2021, **23**(35), 19472–19481, DOI: 10.1039/D1CP03247J.

108 H. Siddique, Z. Xu, X. Li, S. Saeed, W. Liang, X. Wang, C. Gao, R. Dai, Z. Wang and Z. Zhang, Anomalous Octahedron Distortion of Bi-Alloyed $Cs_2AgInCl_6$ Crystal *via* XRD, Raman, Huang–Rhys Factor, and Photoluminescence, *J. Phys. Chem. Lett.*, 2020, **11**(22), 9572–9578, DOI: 10.1021/acs.jpclett.0c02852.

109 D. M. Yost, C. C. Steffens and S. T. Gross, The Raman Spectra and Molecular Constants of the Hexafluorides of Sulfur, Selenium and Tellurium, *J. Chem. Phys.*, 1934, **2**(6), 311–316, DOI: 10.1063/1.1749479.

110 H. Siddique, Z. Xu, X. Li, S. Saeed, W. Liang, X. Wang, C. Gao, R. Dai, Z. Wang and Z. Zhang, Anomalous Octahedron Distortion of Bi-Alloyed $Cs_2AgInCl_6$ Crystal *via* XRD, Raman, Huang–Rhys Factor, and Photoluminescence, *J. Phys. Chem. Lett.*, 2020, **11**(22), 9572–9578, DOI: 10.1021/acs.jpclett.0c02852.

111 J. E. F. S. Rodrigues, C. A. Escanhoela, B. Fragoso, G. Sombrio, M. M. Ferrer, C. Álvarez-Galván, M. T. Fernández-Díaz, J. A. Souza, F. F. Ferreira, C. Pecharromán and J. A. Alonso, Experimental and Theoretical Investigations on the Structural, Electronic, and Vibrational Properties of $Cs_2AgSbCl_6$ Double Perovskite, *Ind. Eng. Chem. Res.*, 2021, **60**(51), 18918–18928, DOI: 10.1021/acs.iecr.1c02188.

112 S. F. Pugh, XCII. Relations between the elastic moduli and the plastic properties of polycrystalline pure metals, *London, Edinburgh Dublin Philos. Mag. J. Sci.*, 2009, **45**(367), 823–843, DOI: 10.1080/14786440808520496.

113 X.-Q. Chen, H. Niu, D. Li and Y. Li, Modeling hardness of polycrystalline materials and bulk metallic glasses, *Intermetallics*, 2011, **19**(9), 1275–1281, DOI: 10.1016/j.intermet.2011.03.026.

114 A. Yangthaisong, First-Principles Study of Electronic, Elastic, and Lattice Vibrational Properties of Pbnm Orthorhombic $SrHfO_3$, *J. Electron. Mater.*, 2013, **42**(6), 993–998, DOI: 10.1007/s11664-013-2492-4.

115 R. Gaillac, P. Pullumbi and F. X. Coudert, ELATE: An Open-Source Online Application for Analysis and Visualization of Elastic Tensors, *J. Phys.: Condens. Matter*, 2016, **28**(27), 275201, DOI: 10.1088/0953-8984/28/27/275201.

116 S. K. S. Saravana Karthikeyan, P. Santhoshkumar, Y. C. Joe, S. H. Kang, Y. N. Jo, H. S. Kang and C. W. Lee, Understanding of the Elastic Constants, Energetics, and Bonding in Dicalcium Silicate Using First-Principles Calculations, *J. Phys. Chem. C*, 2018, **122**(42), 24235–24245, DOI: 10.1021/acs.jpcc.8b06630.

117 S. G. Ramaraj, S. K. Sks, F. Zhang, X. Liu and C. Y. Kong, First-Principles Calculations to Investigate Coupling Fe Doping with Oxygen Vacancies in Stannic Oxide and Their Physical Properties, *J. Phys. Chem. C*, 2023, **127**(27), 13414–13427, DOI: 10.1021/acs.jpcc.3c03627.

118 S. G. Ramaraj, S. K. Sks, F. zhang, X. Liu and C. Y. I. Kong, Electronic, elastic properties and thermal conductivity of the major clinker phases of portland cement: Insights from first-principles calculations, *Vacuum*, 2023, **215**, 112340, DOI: 10.1016/j.vacuum.2023.112340.

119 G. A. Slack, Nonmetallic crystals with high thermal conductivity, *J. Phys. Chem. Solids*, 1973, **34**(2), 321–335, DOI: 10.1016/0022-3697(73)90092-9.

120 Z. Zhang, Y. Jiao, S. K. S. Saravana Karthikeyan, S. G. Ramaraj, F. Zhang, N. Nguyen Dang, X. Qin and X. Liu, First-Principles Calculations to Investigate the Structural, Electronic, Optical, and Elastic Constants; Thermal Conductivity; Raman Scattering; Mulliken Population; and XPS Loss Features of Boron Nitride Polytypes, *J. Phys. Chem. C*, 2023, **127**(34), 17213–17230, DOI: 10.1021/acs.jpcc.3c04086.

121 H. Xie, S. Hao, S. Cai, T. P. Bailey, C. Uher, C. Wolverton, V. P. Dravid and M. G. Kanatzidis, Ultralow thermal conductivity in diamondoid lattices: high thermoelectric performance in chalcopyrite $Cu_{0.8+y}Ag_{0.2}In_{1-y}Te_2$, *Energy Environ. Sci.*, 2020, **13**(10), 3693–3705, DOI: 10.1039/D0EE02323J.

122 Y. Sun, Y. Liu, R. Li, Y. Li and S. Bai, Strategies to improve the thermoelectric figure of merit in thermoelectric functional materials, *Front. Chem.*, 2022, **10**, 865281, DOI: 10.3389/fchem.2022.865281.

123 Q. Ma, G. Ren, K. Xu and J. Z. Ou, Tunable optical properties of 2D materials and their applications, *Adv. Opt. Mater.*, 2021, **9**(2), 2001313, DOI: 10.1002/adom.202001313.

124 A. M. Jafar, K. A. Khalaph and H. B. Al Husseini, Study of the Structural, Electronic, Mechanical, Electro-Thermal and Optical Properties of Double Perovskite Structures Cs_2SbAgX_6, (X = I, Br, or Cl), *Phys. Scr.*, 2022, **97**(8), 085509, DOI: 10.1088/1402-4896/ac8189.

125 E. Haque and M. A. Hossain, Origin of Ultra-Low Lattice Thermal Conductivity in Cs_2BiAgX_6 (X= Cl, Br) and its Impact on Thermoelectric Performance, *J. Alloys Compd.*, 2018, **748**, 63–72, DOI: 10.1016/j.jallcom.2018.03.137.

126 G. Murtaza, Investigation of the Lead-Free Double Perovskites Cs_2AgSbX_6 (X = Cl, Br, I) for Optoelectronic and

Thermoelectric Applications, *arXiv*, 2020, preprint, arXiv:2008.06384, DOI: 10.48550/arXiv.2008.06384.

127 N. H. Alotaibi, Frist principle study of double perovskites Cs_2AgSbX_6 (X = Cl, Br, I) for solar cell and renewable energy applications, *J. Phys. Chem. Solids*, 2022, **1**(171), 110984, DOI: 10.1016/j.jpcs.2022.110984.

128 S. Alnujaim, A. Bouhemadou, M. Chegaar, A. Guechi, S. Bin-Omran, R. Khenata, Y. Al-Douri, W. Yang and H. Lu, Density Functional Theory Screening of Some Fundamental Physical Properties of $Cs_2InSbCl_6$ and $Cs_2InBiCl_6$ Double Perovskites, *Eur. Phys. J. B*, 2022, **95**(7), 114, DOI: 10.1140/epjb/s10051-022-00381-2.

Open Access Article. Published on 07 November 2023. Downloaded on 3/15/2026 12:58:03 PM.
This article is licensed under a Creative Commons Attribution 3.0 Unported Licence.

 This journal is © the Owner Societies 2023